Electronic Supplementary Material (ESI) for ChemComm.

Electronic Supporting Information: Large Vibrationally Induced Parity Violation Effects in CHDBrI$^+$

Eduardus,[†] Yuval Shagam,[‡] Arie Landau,[¶] Shirin Faraji,[§] Peter Schwerdtfeger,[‖] Anastasia Borschevsky,[†] and Lukáš F. Pašteka[*,†,⊥]

[†]*Van Swinderen Institute for Particle Physics and Gravity (VSI), University of Groningen, Groningen, The Netherlands*

[‡]*Schulich Faculty of Chemistry, Solid State Institute and The Helen Diller Quantum Center, Technion-Israel Institute of Technology, Haifa 32000, Israel*

[¶]*Schulich Faculty of Chemistry, The Helen Diller Quantum Center and The Institute of Advanced Studies in Theoretical Chemistry, Technion-Israel Institute of Technology, Haifa 32000, Israel*

[§]*Zernike Institute for Advanced Materials, Faculty of Science and Engineering, University of Groningen, Nijenborgh 4, 9747AG Groningen The Netherlands*

[‖]*Centre for Theoretical Chemistry and Physics, The New Zealand Institute for Advanced Study, Massey University Auckland, Private Bag 102904, 0632 Auckland, New Zealand*

[⊥]*Department of Physical and Theoretical Chemistry, Faculty of Natural Sciences, Comenius University, Mlynská dolina, 84215 Bratislava, Slovakia*

E-mail: l.f.pasteka@rug.nl

In this supporting information, we provide additional data for the geometries, vibrational harmonic and anharmonic treatment of CH_2BrI, CHDBrI, CH_2BrI^+ and $CHDBrI^+$ using vibrational perturbaton theory[1–4] and a few selected density functionals, as well as for parity violation (PV) contributions calculated using the CAMB3LYP* functional,[5] as described in Section S1. Data in Sections S2 – S4 are presented in order to validate the methodology used in optimization, vibrational analysis and PV calculation, respectively, with respect to different levels of theory as well as experimental data available for CH_2BrI. Data in Sections S5 – S8 are presented as further analysis of the parity violation effects in CH_2BrI^+ and $CHDBrI^+$.

S1. Computational Details

Geometry optimization and frequency analyses for CHDBrI and $CHDBrI^+$ were carried out in Q-Chem 5.2.2[6] program package using the ωB97M-V density functional[7] together with Def2-QZVPPD basis set.[8] In the case of iodine the core was replaced by a scalar relativistic Stuttgart pseudopotential. Calculations using the PBE, PB86, B3LYP, MN15 and ωB97X-D functionals were performed in Gaussian 16.[9] CCSD(T) calculations were performed in Molpro 2021.2.0.[10]

Displacement vectors from the vibrational normal modes were used to determine the potential energy $V(q)$ from 11 evenly spaced points q_i between –0.5 Å and 0.5 Å. Along the normal mode, the PV energy contributions were obtained. For this we used the PV Hamiltonian as derived from a Z boson exchange between the electrons and nucleons given by[11]

$$\hat{H}_{\mathrm{PV}} = \frac{G_{\mathrm{F}}}{2\sqrt{2}} \sum_{A}^{\text{nuclei}} Q_{\mathrm{w}}(A) \sum_{i}^{\text{electrons}} \gamma_i^5 \rho_A(\vec{R}_A - \vec{r}_i). \tag{S1}$$

Here, G_{F}=2.22255×10^{-14} a.u. is the Fermi coupling constant, $Q_{\mathrm{w}}(A)$=$(1-4\sin^2\theta_{\mathrm{W}})Z_A - N_A$ the weak charge of nucleus A, θ_{W}=0.2312 the Weinberg mixing angle, and Z_A and N_A are the numbers of protons and neutrons inside nucleus A respectively. γ_i^5 is the Dirac γ^5-matrix

in the standard representation and $\rho_A(\vec{r})$ the nuclear charge density.

The PV energy shift is given by the expectation value $E^{\mathrm{PV}}(q) = \left\langle \Psi^{\mathrm{el}}(q) \right| H^{\mathrm{PV}}(q) \left| \Psi^{\mathrm{el}}(q) \right\rangle$ along a specific normal coordinate $q(\vec{R}_A)$ (see Figure 1 in the main paper). Because of the structure of the PV operator, the PV energy shift can be broken down into the individual atomic contributions, $E^{\mathrm{PV}}(q) = \sum_A E_A^{\mathrm{PV}}(q)$, required for a more detailed analysis. Within mean field theory such as Kohn–Sham, the contributions can be further broken down into the ones coming from the individual molecular orbitals $\sum_i \left\langle \phi_i^{\mathrm{el}}(q) \right| \hat{H}^{\mathrm{PV}}(i,q) \left| \phi_i^{\mathrm{el}}(q) \right\rangle$, where ϕ_i are the occupied Kohn–Sham orbitals.

The $E^{\mathrm{PV}}(q)$ values are obtained from relativistic density functional calculations using X2C/AMFI[12,13] Hamiltonian and the CAM-B3LYP* functional tailored for PV calculations,[5] combined with the augmented uncontracted relativistic Dyall.av4z basis set[14] in DIRAC23 program package.[15] To treat the open-shell cationic species, we have used the average-of-configurations (AOC) formalism in noncollinear approximation.

To generate the PV shift for a specific vibrational mode $|n\rangle$ we used the numerical Numerov–Cooley (NC) procedure[16–18] as well as vibrational perturbation theory (VPT) for interpretational purposes, i.e. along a vibrational normal coordinate q we obtain for a single normal mode up to the linear term in $(n + \frac{1}{2})$,[19]

$$\begin{aligned} E_n^{\mathrm{PV}} &= \langle n(q)| \hat{H}^{\mathrm{PV}}(q) |n(q)\rangle \\ &= E^{\mathrm{PV}}(q=0) + E^{\mathrm{PV}}_{\mathrm{curvature}} + E^{\mathrm{PV}}_{\mathrm{anharmonic}} \\ &= E^{\mathrm{PV}}(q=0) + \frac{\hbar}{\mu\omega_e} \left(\left.\frac{\partial^2 E^{\mathrm{PV}}(q)}{\partial q^2}\right|_{q=0} - \frac{1}{\mu\omega_e^2} \left.\frac{\partial E^{\mathrm{PV}}(q)}{\partial q}\right|_{q=0} \left.\frac{\partial^3 V}{\partial q^3}\right|_{q=0} \right) \left(n + \frac{1}{2}\right), \end{aligned} \tag{S2}$$

where $V(q)$ is the potential energy along the normal coordinate and ω_e is the harmonic vibrational frequency. We call the first term in Eq. (S2) the PV curvature term and the second one the anharmonicity term. Both the potential $V(q)$ and PV energy contribution $E^{\mathrm{PV}}(q)$ for one of the enantiomers are fitted to a polynomial up to the sixth order. We carefully checked the numerical procedures for stability. However, there are some modes

which lead to second derivatives $\partial^2 E^{\mathrm{PV}}/\partial q^2$ close to zero where it was difficult to accurately predict this value. The PV energy difference for the vibrational transitions of the two enantiomers (S, R) is given by $\Delta E^{\mathrm{PV}}_{n\to n'} = (E^{\mathrm{R,PV}}_{n\to n'} - E^{\mathrm{S,PV}}_{n\to n'}) = 2E^{\mathrm{R,PV}}_{n\to n'}$, and similarly for the PV contribution to the vibrational (anharmonic) transition we have $h\Delta\nu^{\mathrm{PV}}_{n\to n'} = \Delta E^{\mathrm{PV}}_{n\to n'}$.

The selected computational methodology was benchmarked against other DFT functionals, CCSD(T) and available experimental data for structural parameters and vibrational frequencies of CH_2BrI, CHDBrI, CH_2BrI^+ and $CHDBrI^+$. The sensitivity of the vibrational PV shift to the level of theory was also tested. Details can be found in the following sections.

From the theoretical point of view, further improvements on the accuracy of the predicted PV shift can be achieved by using a high-accuracy method for treatment of correlation, such as the relativistic coupled cluster approach and by performing a multi-mode PV analysis,[20] both of which are however computationally very demanding.

S2. Geometries

Table S1 summarizes the optimized bond distances and angles for CH_2BrI and CH_2BrI^+ and dipole moments for CH_2BrI, obtained with different DFT functionals and the Def2-QZVPPD basis set.[8] We have also performed geometry optimization using the coupled cluster approach with single, double, and perturbative triple excitations (CCSD(T)) with 40 (39) correlatied electrons (corresponding to the frozen core approximation up to –5 a.u.). As can be seen, the ωB97M-V functional[7] bond lengths and angles are in excellent agreement with the results obtained using CCSD(T) and also compare well to the experimentally derived r_0-structural parameters of CH_2BrI.[21]

We note that for the positively charged species care has to be taken as the geometry opimization may lead to a minimum with the hole, caused by the removal of an electron, being artificially localized at the iodine atom. This state lies 0.0123 a.u. (32 kJ/mol) above the global minimum where the hole is partially delocalized over both halogen atoms. This

artificial localization leads to unreasonable values for the vibrational spectrum and intensities in the lower frequency range and should therefore to be avoided.

Table S1: Equilibrium bond lengths r_e (in Å), bond angles α (in degrees), and dipole moments (in Debye, neutral molecule only) for CH_2BrI and CH_2BrI^+ obtained from various DFT and CCSD(T) calculations and compared to experimentally derived parameters.[21]

Molecule	Property	PBE	PB86	B3LYP	ωB97X-D	ωB97M-V	CCSD(T)	Exp.[a]
CH_2BrI	r_e(CH)	1.090	1.089	1.080	1.081	1.080	1.082	(1.083)
	r_e(CBr)	1.940	1.946	1.943	1.926	1.923	1.923	1.926
	r_e(CI)	2.150	2.156	2.150	2.125	2.121	2.123	(2.131)
	α(HCH)	112.4	112.5	112.2	111.4	111.5	111.9	107.7
	α(HCBr)	107.8	107.8	107.7	107.9	108.0	108.0	107.3
	α(HCI)	107.0	107.0	107.1	107.6	107.7	107.5	–
	α(BrCI)	114.9	114.9	114.9	114.6	113.9	113.9	113.5
	μ_e	1.262	1.277	1.309	1.327	1.321	1.318	–
CH_2BrI^+	r_e(CH)	1.091	1.091	1.081	1.082	1.080	1.084	–
	r_e(CBr)	1.939	1.944	1.937	1.921	1.917	1.922	–
	r_e(CI)	2.143	2.151	2.146	2.118	2.115	2.120	–
	α(HCH)	116.4	116.5	116.1	115.6	115.6	116.5	–
	α(HCBr)	111.1	111.0	111.1	111.4	111.9	111.4	–
	α(HCI)	110.8	110.7	110.6	111.3	110.7	111.0	–
	α(BrCI)	94.5	94.8	95.4	93.7	94.1	93.1	–

[a] r_0-structure derived from isotopic substitution rotational spectra. Numbers in parentheses were fixed to *ab initio* data in the fitting procedure.

S3. Vibrational Analysis

Tables S2–S5 summarize the calculated harmonic and anharmonic vibrational frequencies, intensities and lifetimes for the different molecules at different levels of density functional theory using vibrational perturbation theory. Modes 1 to 7 are fairly harmonic in their nature (see Figure S3) and thus the harmonic approximation introduces only a relatively small error in vibrational frequencies compared to the anharmonic results (< 40 cm^{-1}). The C–H/D stretching modes 8 and 9 are the most anharmonic and the error of the harmonic

approximation is also the largest ($100 - 200\,\mathrm{cm}^{-1}$). For CH_2BrI the smallest root mean square deviation from experiment[22,23] is obtained for the B3LYP and ωB97M-V functionals.[7]

For the radical cationic systems, the open-shell formalism potentially plays a significant role in the correct description of the electronic structure. We therefore calculated the main species of interest, $CHDBrI^+$, with UKS as well as ROKS formalism using two functionals (ωB97X-D and MN15), two basis sets (Def2-QZVPPD, Def2-TZVP), and two optimization point groups (C_s and C_1). The results are collected in Table S6 and Figure S1 below. The $V(q)$ curves are virtually indistinguishable and harmonic frequencies agree to a very high degree. While still small, the largest effect is that of the DFT functional ($< 1\%$). Interestingly, while the effect of the DFT functional grows with the mode frequency, the effect of the open-shell formalism exhibits an opposite trend – the UKS and ROKS frequencies agree within 0.01% for the highest mode and within 0.3% for the lowest.

In Figure S2, we show comparison of the $V(q)$ curves obtained from fully relativistic DIRAC calculations and pseudo-relativistic (ECP) Q-Chem calculations as described in Section S1. Both were calculated in the same set of displaced geometries based on the harmonic vibrational analysis performed in Q-Chem. As can be seen from the plots, the potentials between the two computational approaches agree to a high degree. Qualitative agreement can be observed for all modes. For most modes, we can also confirm quantitative agreement, except for vibrational mode 1, for which the DIRAC potential is somewhat shifted with respect to the Q-Chem potential. In all evaluations of vibrational wavefunctions we use the Q-Chem potentials as these are based on the Q-Chem optimized structure and harmonic analysis.

Table S2: Vibrational harmonic (harm) and anharmonic (anharm) fundamental transition frequencies (in cm^{-1}) for the molecules CH_2BrI, CH_2BrI^+, CHDBrI, and $CHDBrI^+$ obtained from a 3-mode analysis.

Mode	PBE harm	PBE anharm	PB86 harm	PB86 anharm	B3LYP harm	B3LYP anharm	ωB97X-D harm	ωB97X-D anharm	ωB97M-V harm	ωB97M-V anharm	Exp. [22,23]
CH_2BrI											
1	136.3	136.0	135.3	136.6	140.2	143.3	145.9	143.0	146.4	144.9	144
2	508.9	499.7	503.1	493.2	515.1	505.3	545.0	535.0	548.4	540.8	517
3	599.2	582.3	588.6	572.6	608.2	593.4	663.2	644.2	671.2	652.9	616
4	739.2	732.4	738.9	732.3	764.6	757.7	775.3	767.5	774.5	763.4	754
5	1047.6	1030.0	1046.9	1028.1	1089.4	1072.2	1112.0	1078.4	1107.4	1087.6	1065
6	1126.4	1106.8	1127.5	1107.8	1178.3	1159.3	1200.1	1163.1	1191.9	1168.1	1150
7	1368.3	1328.7	1370.0	1329.3	1426.0	1386.0	1441.5	1402.6	1433.9	1369.7	1374
8	3059.5	2933.7	3052.6	2924.6	3133.4	3009.7	3148.4	2957.4	3151.2	3019.3	2978
9	3147.9	3002.0	3141.8	2994.4	3220.8	3077.0	3233.6	3021.3	3232.6	3083.5	3091
RMSD	37.7	42.6	35.7	46.6	72.9	17.4	84.9	28.9	84.6	24.4	
CH_2BrI^+											
1	135.6	134.9	133.9	138.7	137.0	128.4	153.3	159.9	152.3		
2	515.3	493.3	505.3	485.0	509.4	487.9	551.0	535.8	538.5		
3	603.2	585.3	594.1	582.9	605.8	589.2	645.7	637.4	651.0		
4	794.3	790.9	793.9	788.5	821.9	813.6	837.4	827.5	835.3		
5	981.9	963.0	981.8	965.5	1020.9	997.9	1033.9	1029.6	1028.7		
6	1095.3	1073.9	1096.7	1079.1	1140.7	1119.3	1154.5	1146.9	1143.9		
7	1361.5	1324.4	1363.4	1327.2	1417.5	1378.0	1431.7	1396.0	1422.5		
8	3054.6	2930.8	3048.0	2925.0	3129.8	3008.3	3145.6	3000.3	3150.9		
9	3168.1	3027.9	3162.6	3020.5	3242.2	3101.4	3256.8	3089.5	3259.7		
CHDBrI											
1	136.0	128.6	135.0	129.4	139.9	139.8	145.6	130.9	146.3		
2	492.0	478.5	486.6	476.5	498.1	488.2	525.6	513.5	539.5		
3	583.8	564.9	574.1	558.0	592.8	577.1	641.0	618.7	644.6		
4	636.9	627.4	636.2	629.1	658.0	650.9	669.3	658.2	679.2		
5	790.8	771.4	789.8	774.4	823.8	809.4	847.0	817.9	845.1		
6	1090.1	1064.2	1090.6	1067.7	1138.3	1117.6	1161.1	1117.0	1155.6		
7	1217.3	1183.2	1218.8	1185.8	1268.3	1235.1	1281.8	1248.4	1283.9		
8	2276.5	2202.1	2271.7	2197.5	2330.7	2259.6	2341.2	2237.2	2345.8		
9	3106.8	2965.8	3100.3	2958.0	3180.1	3042.5	3193.8	2989.1	3198.0		
$CHDBrI^+$											
1	135.4	136.1	133.7	128.3	136.8	130.9	153.1	149.0	149.1		
2	499.1	481.4	490.2	471.0	494.9	476.6	532.3	517.5	524.4		
3	582.4	570.7	574.4	560.4	585.9	572.2	620.6	607.2	619.8		
4	674.2	668.8	673.0	663.8	696.7	689.6	713.8	702.5	709.9		
5	755.9	744.5	755.0	738.3	783.7	769.1	797.1	787.6	796.5		
6	1047.3	1029.8	1048.1	1026.6	1090.2	1073.2	1104.8	1091.4	1103.8		
7	1216.2	1188.0	1217.8	1185.7	1265.9	1233.3	1279.0	1247.0	1274.9		
8	2281.5	2211.5	2277.0	2204.2	2336.7	2266.3	2348.4	2263.2	2354.0		
9	3116.3	2982.6	3110.3	2973.2	3190.8	3057.3	3205.9	3044.9	3213.8		

Table S3: Harmonic (harm) and anharmonic (anharm) IR intensities (in km/mol) for the fundamental transitions of the molecules CH_2BrI, CH_2BrI^+, CHDBrI, and $CHDBrI^+$ obtained from a 3-mode analysis.

Mode	PBE harm	PBE anharm	PB86 harm	PB86 anharm	B3LYP harm	B3LYP anharm	ωB97X-D harm	ωB97X-D anharm	ωB97M-V harm
CH_2BrI									
1	0.041	0.039	0.040	0.038	0.059	0.057	0.110	0.108	0.105
2	8.984	11.510	10.473	13.226	6.547	8.337	2.372	2.552	2.873
3	83.097	84.491	86.608	87.923	78.170	80.713	57.181	60.437	54.843
4	5.027	4.809	4.902	4.680	4.900	4.722	5.114	4.956	4.636
5	0.021	0.071	0.017	0.034	0.009	0.024	0.005	0.012	0.003
6	69.195	61.932	72.708	65.203	81.769	74.460	73.784	58.873	74.952
7	0.002	0.026	0.024	0.037	0.034	0.051	0.032	0.035	0.006
8	0.367	1.102	0.435	1.282	0.409	1.202	0.478	0.940	0.821
9	4.110	1.964	3.691	1.682	3.957	1.915	3.919	2.406	3.249
CH_2BrI^+									
1	0.457	0.433	0.420	0.395	0.874	0.834	1.963	1.860	3.410
2	13.617	13.988	14.279	15.330	17.277	18.359	20.046	21.082	25.556
3	7.084	7.140	7.563	7.944	7.540	7.980	7.024	7.345	7.240
4	2.400	2.296	2.316	2.196	2.364	2.275	2.599	2.643	2.224
5	0.023	0.003	0.020	0.041	0.021	0.018	0.017	0.067	0.037
6	1.168	0.852	1.298	1.037	1.071	0.902	0.947	0.886	1.044
7	0.472	0.502	0.485	0.467	0.769	0.737	0.780	0.844	1.273
8	15.139	13.982	14.298	12.129	13.878	12.050	14.524	13.164	13.156
9	28.178	25.571	27.222	22.979	27.985	24.190	29.027	25.828	28.327
CHDBrI									
1	0.042	0.039	0.041	0.039	0.060	0.059	0.110	0.109	0.066
2	6.855	7.705	8.020	9.483	5.078	6.063	1.865	1.820	1.547
3	67.849	68.891	72.167	74.428	63.683	66.744	40.530	41.530	37.709
4	2.575	2.427	2.499	2.365	2.503	2.415	2.694	2.510	2.393
5	35.292	33.735	35.548	32.982	35.912	34.211	34.834	33.857	35.663
6	43.512	39.993	45.825	41.467	51.858	45.290	47.063	39.287	47.343
7	1.116	0.798	1.110	0.939	1.135	1.088	1.117	0.781	1.007
8	1.044	0.936	0.981	0.950	1.031	1.074	1.048	1.314	1.030
9	2.447	1.536	2.247	1.502	2.375	1.579	2.377	1.734	2.125
$CHDBrI^+$									
1	0.455	0.437	0.417	0.396	0.871	0.836	1.961	1.839	4.373
2	11.503	12.551	12.197	13.291	15.088	16.256	17.054	18.310	21.834
3	6.143	6.557	6.598	6.952	6.680	7.007	6.079	5.966	6.490
4	1.970	1.922	1.934	1.896	1.947	1.938	2.332	2.836	2.284
5	1.548	1.254	1.546	1.370	1.342	1.207	1.716	1.485	2.049
6	1.034	0.811	1.149	0.856	0.955	0.762	0.795	0.672	0.746
7	1.002	0.942	1.043	0.949	1.327	1.151	1.303	1.297	1.790
8	8.438	7.114	7.940	6.556	7.948	6.688	8.445	7.412	7.551
9	22.438	19.055	21.539	18.010	21.754	18.461	22.602	19.943	20.723

Table S4: Harmonic (harm) and anharmonic (anharm) lifetimes for the fundamental transitions of the molecules CH_2BrI, CH_2BrI^+, CHDBrI, and $CHDBrI^+$ obtained from a 3-mode analysis.

Mode	PBE harm	PBE anharm	PB86 harm	PB86 anharm	B3LYP harm	B3LYP anharm	ωB97X-D harm	ωB97X-D anharm	ωB97M-V harm
CH_2BrI									
1	2.91 h	3.08 h	3.03 h	3.13 h	1.91 h	1.9 h	56.9 min	1.01 h	59.2 min
2	3.44 s	2.78 s	3.02 s	2.48 s	4.6 s	3.75 s	11.3 s	10.9 s	9.25 s
3	268 ms	279 ms	266 ms	277 ms	276 ms	281 ms	318 ms	319 ms	323 ms
4	2.91 s	3.1 s	2.99 s	3.18 s	2.79 s	2.95 s	2.6 s	2.74 s	2.87 s
5	5.78 min	1.77 min	7.15 min	3.71 min	12.5 min	4.83 min	21.5 min	9.55 min	36.2 min
6	91 ms	105 ms	86.5 ms	99.9 ms	70.4 ms	79.9 ms	75.2 ms	100 ms	75.1 ms
7	35.6 min	2.9 min	2.96 min	2.04 min	1.93 min	1.36 min	2 min	1.93 min	10.8 min
8	2.33 s	843 ms	1.97 s	729 ms	1.99 s	734 ms	1.69 s	972 ms	980 ms
9	196 ms	452 ms	219 ms	530 ms	195 ms	441 ms	195 ms	364 ms	235 ms
CH_2BrI^+									
1	15.9 min	16.9 min	17.7 min	17.5 min	8.12 min	9.69 min	2.89 min	2.8 min	1.68 min
2	2.21 s	2.35 s	2.19 s	2.22 s	1.78 s	1.83 s	1.31 s	1.32 s	1.08 s
3	3.1 s	3.27 s	2.99 s	2.96 s	2.89 s	2.89 s	2.73 s	2.68 s	2.6 s
4	5.28 s	5.57 s	5.48 s	5.85 s	5.01 s	5.31 s	4.39 s	4.42 s	5.15 s
5	6.01 min	47.9 min	6.91 min	3.49 min	6.09 min	7.43 min	7.33 min	1.88 min	3.4 min
6	5.7 s	8.13 s	5.12 s	6.62 s	5.74 s	7.07 s	6.33 s	6.86 s	5.85 s
7	9.14 s	9.08 s	8.87 s	9.72 s	5.17 s	5.71 s	5 s	4.86 s	3.1 s
8	56.6 ms	66.6 ms	60.2 ms	77 ms	58.8 ms	73.3 ms	55.6 ms	67.4 ms	61.2 ms
9	28.3 ms	34.1 ms	29.4 ms	38.1 ms	27.2 ms	34.4 ms	26 ms	32.4 ms	26.6 ms
CHDBrI									
1	2.86 h	3.44 h	2.97 h	3.4 h	1.89 h	1.93 h	57.1 min	1.19 h	1.57 h
2	4.82 s	4.53 s	4.21 s	3.71 s	6.34 s	5.53 s	15.5 s	16.7 s	17.8 s
3	346 ms	364 ms	336 ms	345 ms	357 ms	360 ms	480 ms	503 ms	510 ms
4	7.65 s	8.37 s	7.9 s	8.54 s	7.38 s	7.81 s	6.62 s	7.35 s	7.24 s
5	362 ms	398 ms	360 ms	404 ms	328 ms	357 ms	320 ms	353 ms	314 ms
6	155 ms	176 ms	147 ms	169 ms	119 ms	141 ms	126 ms	163 ms	126 ms
7	4.83 s	7.15 s	4.85 s	6.05 s	4.38 s	4.82 s	4.36 s	6.57 s	4.82 s
8	1.48 s	1.76 s	1.58 s	1.74 s	1.43 s	1.46 s	1.39 s	1.22 s	1.41 s
9	338 ms	592 ms	370 ms	608 ms	333 ms	547 ms	330 ms	516 ms	368 ms
$CHDBrI^+$									
1	16 min	16.5 min	17.9 min	20.4 min	8.17 min	9.3 min	2.9 min	3.26 min	1.37 min
2	2.79 s	2.75 s	2.73 s	2.71 s	2.16 s	2.16 s	1.65 s	1.63 s	1.33 s
3	3.84 s	3.74 s	3.67 s	3.66 s	3.49 s	3.48 s	3.41 s	3.63 s	3.21 s
4	8.93 s	9.3 s	9.12 s	9.57 s	8.46 s	8.67 s	6.73 s	5.71 s	6.94 s
5	9.04 s	11.5 s	9.07 s	10.7 s	9.7 s	11.2 s	7.33 s	8.68 s	6.15 s
6	7.05 s	9.29 s	6.33 s	8.86 s	7.04 s	9.11 s	8.24 s	9.99 s	8.79 s
7	5.39 s	6.01 s	5.17 s	5.99 s	3.76 s	4.57 s	3.75 s	3.96 s	2.75 s
8	182 ms	230 ms	194 ms	251 ms	184 ms	233 ms	172 ms	211 ms	191 ms
9	36.7 ms	47.2 ms	38.4 ms	50.2 ms	36.1 ms	46.3 ms	34.4 ms	43.2 ms	37.3 ms

Table S5: Overtone ($0 \rightarrow 2$) anharmonic frequencies (in cm^{-1}) and corresponding intensities (in km/mol) for the molecules CH_2BrI, CH_2BrI^+, CHDBrI, and $CHDBrI^+$ obtained from a 3-mode analysis.

Mode	PBE freq	PBE int	PB86 freq	PB86 int	B3LYP freq	B3LYP int	ωB97X-D freq	ωB97X-D int
CH_2BrI								
1	271.8	0.001	273.0	0.000	286.4	0.000	285.9	0.001
2	992.1	0.193	979.1	0.224	1004.4	0.133	1065.5	0.055
3	1154.7	0.404	1135.6	0.420	1178.0	0.355	1278.3	0.177
4	1464.8	0.010	1464.5	0.008	1515.6	0.010	1537.5	0.013
5	2055.9	0.102	2051.3	0.092	2139.9	0.072	2148.8	0.081
6	2207.1	0.766	2208.9	0.763	2311.7	0.645	2314.8	0.545
7	2643.8	0.000	2644.2	0.000	2757.1	0.005	2790.8	0.014
8	5809.8	0.616	5790.4	0.604	5962.1	0.556	5827.6	0.446
9	5934.9	1.219	5918.4	1.221	6085.8	1.176	5944.0	0.968
CH_2BrI^+								
1	269.6	0.001	277.1	0.001	256.5	0.001	318.7	0.003
2	974.3	0.010	958.7	0.007	963.9	0.011	1061.8	0.033
3	1162.0	0.042	1158.7	0.045	1170.9	0.065	1268.7	0.068
4	1583.6	0.027	1578.0	0.027	1628.2	0.033	1651.2	0.037
5	1922.3	0.115	1927.1	0.104	1991.3	0.086	2057.5	0.106
6	2143.3	0.996	2152.3	1.003	2234.0	0.879	2290.2	0.830
7	2635.9	0.140	2641.2	0.144	2741.6	0.140	2777.5	0.139
8	5806.2	0.671	5794.1	0.665	5961.6	0.591	5927.2	0.492
9	5990.1	1.111	5974.5	1.114	6137.9	1.032	6094.8	0.870
CHDBrI								
1	258.0	0.001	258.7	0.000	279.5	0.000	261.7	0.000
2	950.6	0.134	946.5	0.165	970.9	0.107	1023.0	0.038
3	1120.6	0.420	1107.4	0.520	1145.7	0.458	1227.5	0.235
4	1254.7	0.169	1258.3	0.177	1302.7	0.212	1317.5	0.177
5	1535.4	0.182	1541.3	0.174	1612.0	0.141	1623.7	0.133
6	2115.6	0.616	2123.4	0.590	2221.2	0.405	2211.2	0.096
7	2357.1	0.252	2361.8	0.240	2460.2	0.229	2485.3	0.234
8	4339.3	0.635	4328.8	0.628	4454.6	0.603	4363.9	0.498
9	5809.7	1.569	5791.4	1.558	5964.1	1.496	5799.0	1.213
$CHDBrI^+$								
1	271.8	0.001	256.3	0.001	261.7	0.000	296.9	0.003
2	952.1	0.010	931.0	0.005	942.6	0.005	1026.5	0.025
3	1134.9	0.045	1114.1	0.046	1137.6	0.066	1210.0	0.068
4	1337.1	0.126	1326.7	0.127	1378.8	0.137	1399.7	0.126
5	1484.0	0.181	1470.8	0.173	1532.7	0.155	1571.2	0.165
6	2051.3	1.003	2044.0	0.984	2137.4	0.889	2173.7	0.896
7	2367.1	0.732	2362.2	0.702	2456.9	0.670	2483.3	0.680
8	4362.1	0.529	4346.8	0.525	4471.9	0.480	4445.4	0.402
9	5849.8	1.368	5829.8	1.366	6000.1	1.250	5938.9	1.036

Table S6: Comparison of effects of the DFT functional, basis set, optimization point group and open-shell formalism on vibrational harmonic transition frequencies (in cm^{-1}) for $CHDBrI^+$.

Mode	ωB97X-D								MN15			
	Def2-TZVP				Def2-QZVPPD				Def2-TZVP		Def2-QZVPPD	
	C_s		C_1		C_s		C_1		C_s		C_s	
	ROKS	UKS	ROKS	UKS	ROKS	UKS	ROKS	UKS	ROKS	UKS	ROKS	UKS
1	151.4	151.7	151.3	151.6	152.7	153.2	152.6	153.1	151.6	150.9	151.9	151.2
2	534.0	531.7	534.2	531.7	534.6	532.3	534.9	532.4	519.9	517.2	520.6	518.1
3	622.0	620.5	622.1	620.7	622.2	620.7	622.1	620.7	619.9	618.7	621.3	620.1
4	712.6	712.1	712.2	711.9	714.8	713.9	713.9	713.4	699.0	698.5	699.0	698.2
5	797.5	797.1	797.4	797.0	797.5	797.1	797.6	797.0	788.9	788.7	787.5	787.3
6	1105.1	1105.0	1105.1	1105.0	1104.9	1104.7	1105.1	1104.6	1090.9	1091.2	1088.5	1088.5
7	1276.5	1276.2	1276.4	1276.1	1279.3	1279.0	1279.0	1278.8	1261.9	1261.6	1260.9	1260.6
8	2350.7	2350.8	2351.0	2351.1	2348.5	2348.4	2348.6	2348.6	2369.3	2369.3	2364.3	2364.3
9	3209.1	3209.3	3210.7	3210.8	3205.9	3205.9	3206.9	3206.9	3235.0	3235.0	3227.7	3227.6

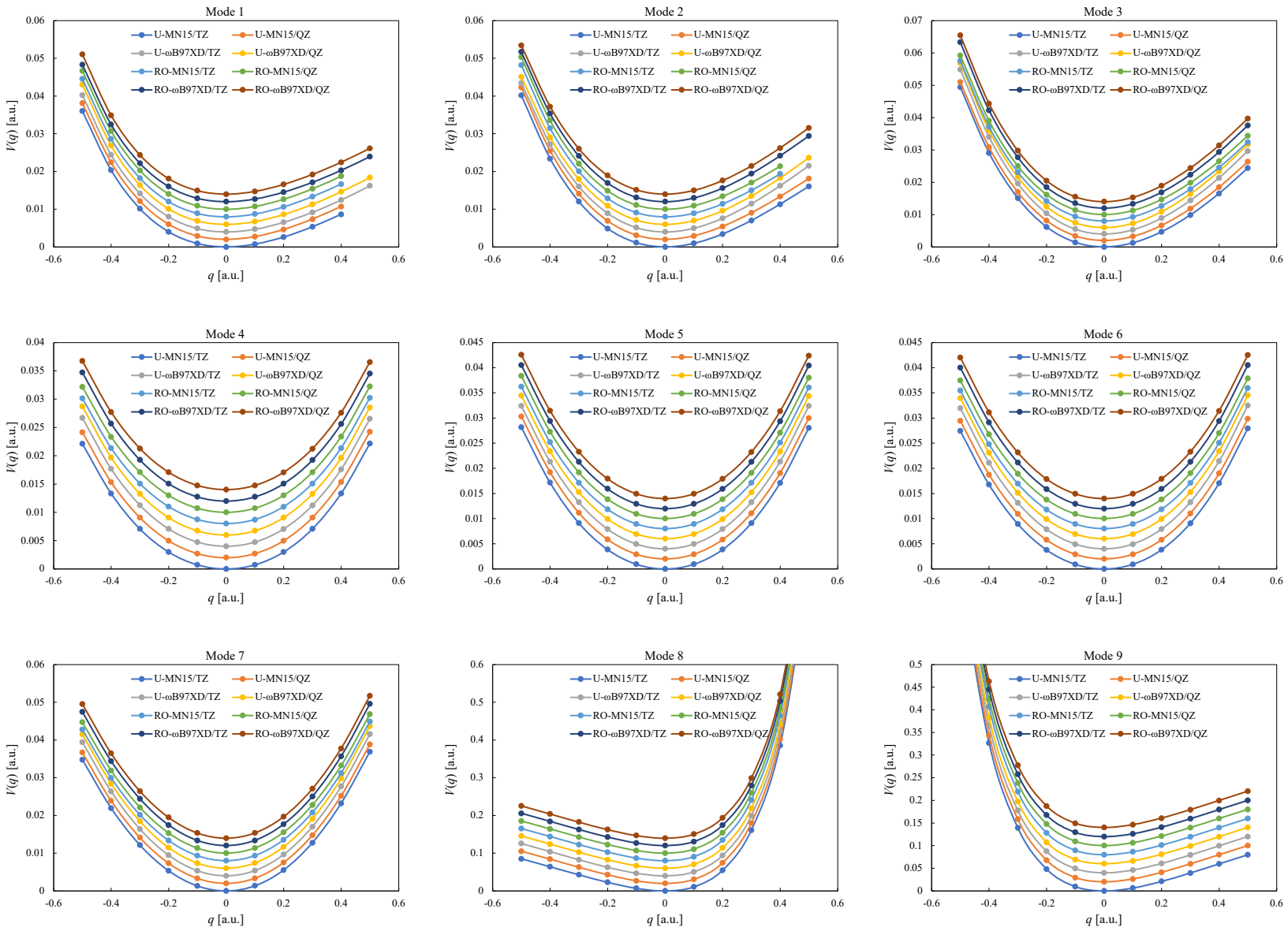

Figure S1: Comparison of effects of the DFT functional, basis set, and open-shell formalism on potential curves $V(q)$ along vibrational modes of $CHDBrI^+$. For visual clarity, the potential curves are vertically shifted using an equidistant step of 0.002 and 0.02 a.u. for modes 1–7 and 8–9, respectively.

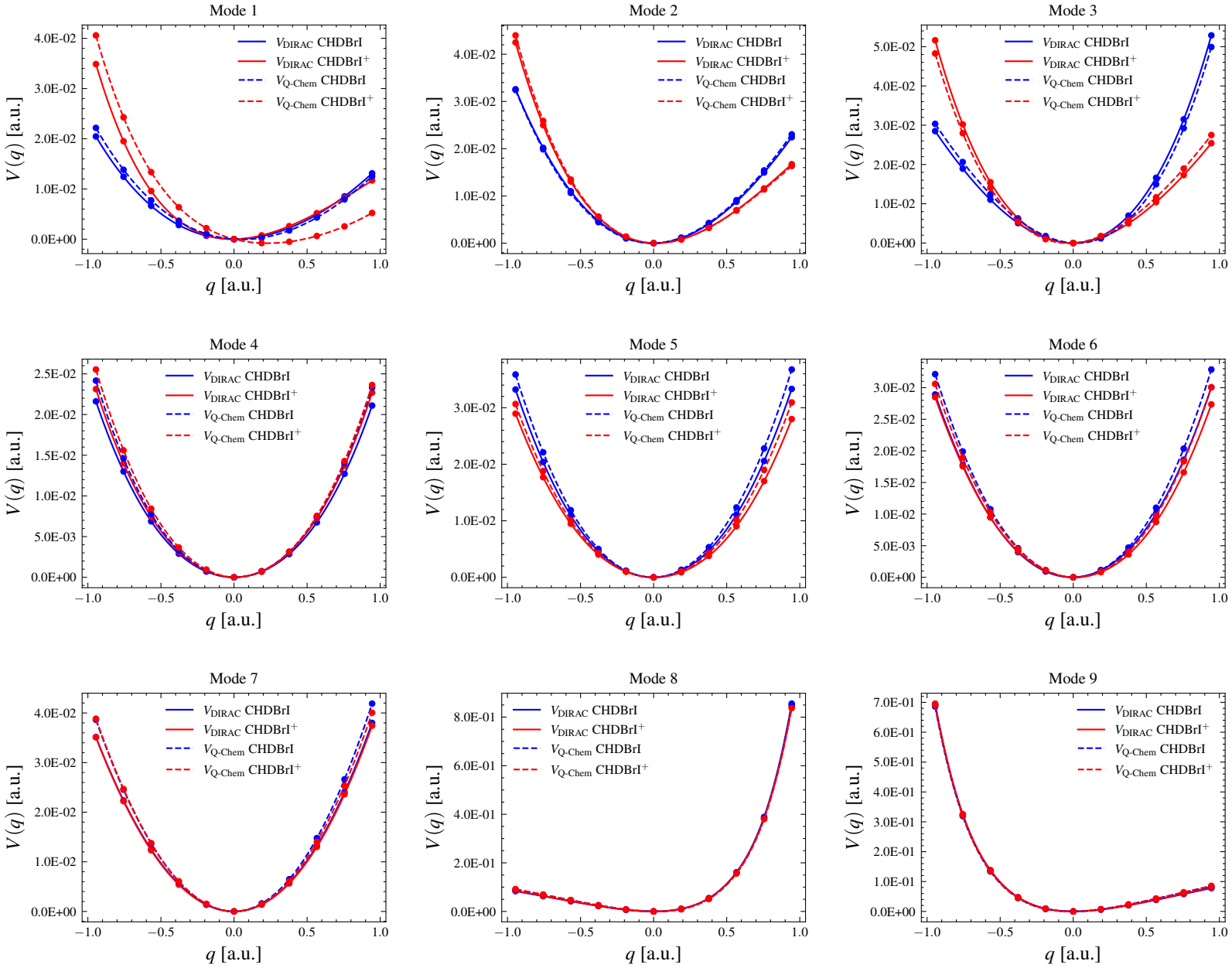

Figure S2: Comparison of potential curves $V(q)$ obtained from DIRAC and Q-Chem calculations (as described in Section S1). In both cases, the displacements q are based on the Q-Chem harmonic analysis.

S4. Dependence of the PV energy shift on the level of theory

The CH wagging mode (mode 6) in $CHDBrI^+$ turns out to be a very promising candidate for future high-precision spectroscopy experiments. Therefore, to ensure the reliability of our theoretical prediction for the magnitude of the PV frequency shift $\Delta\nu^{PV}$ for this mode, we tested the effect of the basis set applied, our computational approach (HF vs. DFT), and the choice of the functional used on our results. From Table S7, we can see that using a smaller basis set (Def2-TZVP) has only a minor effect on the PV frequency difference. Hybrid DFT functionals sit at the intersection of the delocalized LDA and localized HF. By comparing our results to these extremes, we can easily set very conservative bounds on the result without the need to test an entire spectrum of DFT functionals. HF and LDA yield significanly different values. However, the PV frequency shift is still in the ballpark of 1 Hz, which gives confidence for our method used, even in the case when HF was used also for the optimization step. The result can thus be considered fairly robust. We have thoroughly tested the dependence of the result on the parameters of the methodology in our previous work[24] with a similar conclusion.

Table S7: Calculated PV frequency shift $\Delta\nu^{PV}$ (in Hz) for vibrational mode 6 of (R)-$CHDBrI^+$ on different levels of theory (method or functional / basis set). Reference method and result shown in bold.

Geometry optimization	DIRAC calculations	$\Delta\nu^{PV}$
ωB97M-V / Def2-QZVPPD	**CAM-B3LYP* /Dyall.av4z**	**–1.78**
ωB97M-V / Def2-TZVP	CAM-B3LYP* / Dyall.v3z	–1.72
ωB97M-V / Def2-QZVPPD	HF / Dyall.av4z	–1.37
ωB97M-V / Def2-QZVPPD	LDA / Dyall.av4z	–0.86
HF / Def2-QZVPPD	HF / Dyall.av4z	–0.86

S5. Vibrational PV Shift Analysis

Table S8 shows the results of the VPT analysis of the PV energies for all modes. Mode 6 was discussed in the main text. Similarly, modes 5 and 7 are dominated by the harmonic VPT term in Eq. (S2). In contrast, modes 8 and 9 corresponding to the H/D stretching, which are strongly anharmonic, are dominated by the anharmonic VPT term in Eq. (S2).

Figure S3 summarizes potential energy $V(q)$ and PV $E^{\mathrm{PV}}(q)$ curves for all modes of both molecules. This visually supports the VPT analysis in Table S8. For the sake of reproducibility, in Table S8 we provide all calculated datapoints as well as fitting coeficients of the curves shown in the plots in Figure S3.

Table S8: PV value for Numerov–Cooley (NC) procedure and VPT (vibrational perturbation theory) values $\Delta\nu^{\mathrm{PV}}$ (in Hz) for (R)-CHDBrI$^+$. Curvature and anharmonic VPT contributions of from Eq. (S2) are shown separately.

Mode	CHDBrI				CHDBrI$^+$			
number	NC	VPT	VPT curv.	VPT anharm.	NC	VPT	VPT curv.	VPT anharm.
1	–0.0010	–0.0010	–0.0006	0.0004	0.0088	0.0088	0.0054	–0.0035
2	–0.0442	–0.0423	–0.0346	0.0078	–0.1256	–0.1145	–0.0373	0.0772
3	0.2419	0.2347	0.0860	–0.1487	–0.0367	–0.0457	0.2489	0.2946
4	–0.0509	–0.0523	–0.0567	–0.0044	–0.0415	–0.0769	–0.0321	0.0448
5	–0.0614	–0.0649	–0.0490	0.0159	1.3352	1.3452	1.3264	–0.0188
6	0.0534	0.0292	0.0493	0.0200	–1.7789	–1.8421	–1.8405	0.0016
7	0.0428	0.0535	0.0203	–0.0332	–0.5901	–0.6102	–0.5573	0.0529
8	0.0177	0.0194	0.0155	–0.0039	0.9370	0.8541	0.2086	–0.6454
9	–0.0549	–0.0555	–0.0022	0.0533	–1.2918	–1.1562	–0.2159	0.9403

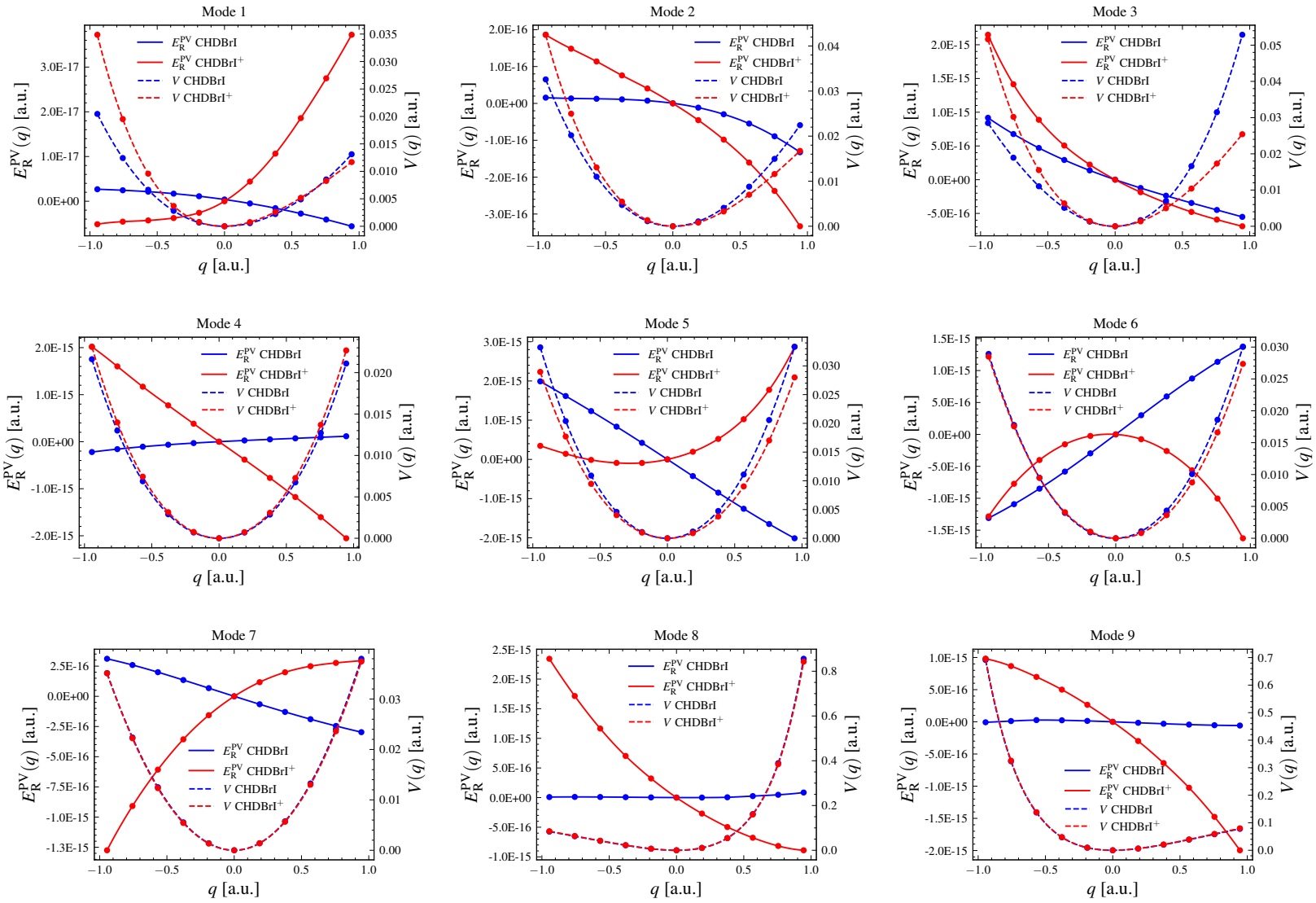

Figure S3: Comparison between (R)-CHDBrI and (R)-CHDBrI$^+$ for the potential energy $V(q)$ and PV $E^{\mathrm{PV}}(q)$ curves.

Table S9: Raw data of the potential energy $V(q)$ and PV $E^{\mathrm{PV}}(q)$ for (R)-CHDBrI and (R)-CHDBrI$^+$, including polynomial fitting coefficients (C_N) for $f(x) = \sum^N C_N x^N$. All energy values for $V(q)$ and $E^{\mathrm{PV}}(q)$ are expressed in a.u..

Mode 1					Mode 2				
	CHDBrI		CHDBrI$^+$			CHDBrI		CHDBrI$^+$	
q[Å]	$V(q)$	$E^{\mathrm{PV}}(q)$	$V(q)$	$E^{\mathrm{PV}}(q)$	q[Å]	$V(q)$	$E^{\mathrm{PV}}(q)$	$V(q)$	$E^{\mathrm{PV}}(q)$
–0.5	2.046E–02	2.679E–18	3.488E–02	–5.138E–18	–0.5	3.259E–02	1.563E–17	4.250E–02	1.862E–16
–0.4	1.243E–02	2.454E–18	1.951E–02	–4.568E–18	–0.4	2.019E–02	1.351E–17	2.498E–02	1.483E–16
–0.3	6.639E–03	2.138E–18	9.580E–03	–4.296E–18	–0.3	1.099E–02	1.255E–17	1.306E–02	1.137E–16
–0.2	2.806E–03	1.699E–18	3.691E–03	–3.758E–18	–0.2	4.715E–03	1.098E–17	5.462E–03	7.593E–17
–0.1	6.730E–04	1.121E–18	7.750E–04	–2.588E–18	–0.1	1.129E–03	7.410E–18	1.346E–03	4.044E–17
0	0	3.905E–19	0	–9.433E–21	0	0	3.905E–19	0	–9.433E–21
0.1	5.690E–04	–4.998E–19	7.550E–04	4.397E–18	0.1	1.072E–03	–1.146E–17	8.120E–04	–4.544E–17
0.2	2.226E–03	–1.549E–18	2.598E–03	1.064E–17	0.2	4.082E–03	–2.940E–17	3.279E–03	–9.818E–17
0.3	4.891E–03	–2.760E–18	5.181E–03	1.858E–17	0.3	8.783E–03	–5.474E–17	6.995E–03	–1.604E–16
0.4	8.524E–03	–4.101E–18	8.255E–03	2.749E–17	0.4	1.496E–02	–8.922E–17	1.159E–02	–2.373E–16
0.5	1.312E–02	–5.600E–18	1.169E–02	3.723E–17	0.5	2.243E–02	–1.324E–16	1.672E–02	–3.332E–16
Fitting Coefficients									
C_6	–2.550E–04	–8.075E–20	3.140E–04	3.946E–18	C_6	3.705E–04	5.063E–18	5.480E–04	–5.102E–18
C_5	2.700E–04	–5.670E–20	–1.365E–03	–1.718E–18	C_5	2.395E–04	1.618E–18	–1.223E–03	–6.528E–18
C_4	1.830E–03	2.858E–19	5.073E–03	–1.226E–17	C_4	–3.591E–04	–4.297E–18	2.795E–03	–8.153E–18
C_3	–4.439E–03	–4.821E–20	–1.302E–02	6.157E–18	C_3	–6.299E–03	–3.501E–17	–1.307E–02	–5.099E–17
C_2	1.738E–02	–2.265E–18	2.130E–02	2.578E–17	C_2	3.084E–02	–6.601E–17	3.024E–02	–7.087E–17
C_1	–1.370E–04	–4.293E–18	4.380E–04	1.829E–17	C_1	5.718E–05	–4.840E–17	–9.980E–04	–2.241E–16
C_0	–1.000E–06	3.913E–19	–2.000E–06	–3.696E–21	C_0	–4.586E–07	3.437E–19	–4.000E–06	–1.558E–19

Mode 3					Mode 4				
	CHDBrI		CHDBrI$^+$			CHDBrI		CHDBrI$^+$	
q[Å]	$V(q)$	$E^{\mathrm{PV}}(q)$	$V(q)$	$E^{\mathrm{PV}}(q)$	q[Å]	$V(q)$	$E^{\mathrm{PV}}(q)$	$V(q)$	$E^{\mathrm{PV}}(q)$
–0.5	2.850E–02	9.173E–16	5.163E–02	2.148E–15	–0.5	2.162E–02	–2.197E–16	2.312E–02	2.019E–15
–0.4	1.893E–02	6.766E–16	3.020E–02	1.415E–15	–0.4	1.301E–02	–1.578E–16	1.399E–02	1.601E–15
–0.3	1.105E–02	4.700E–16	1.550E–02	8.877E–16	–0.3	6.881E–03	–1.065E–16	7.440E–03	1.170E–15
–0.2	5.087E–03	2.922E–16	6.315E–03	5.063E–16	–0.2	2.903E–03	–6.439E–17	3.154E–03	7.727E–16
–0.1	1.297E–03	1.375E–16	1.431E–03	2.232E–16	–0.1	7.010E–04	–2.925E–17	7.680E–04	3.827E–16
0	0	3.905E–19	0	–9.433E–21	0	0	3.905E–19	0	–9.433E–21
0.1	1.683E–03	–1.233E–16	1.360E–03	–1.852E–16	0.1	6.930E–04	2.618E–17	7.400E–04	–3.810E–16
0.2	6.976E–03	–2.374E–16	4.979E–03	–3.430E–16	0.2	2.860E–03	4.962E–17	3.078E–03	–7.704E–16
0.3	1.661E–02	–3.449E–16	1.042E–02	–4.781E–16	0.3	6.751E–03	7.193E–17	7.278E–03	–1.177E–15
0.4	3.149E–02	–4.487E–16	1.731E–02	–5.918E–16	0.4	1.272E–02	9.390E–17	1.370E–02	–1.604E–15
0.5	5.287E–02	–5.512E–16	2.541E–02	–6.905E–16	0.5	2.110E–02	1.162E–16	2.268E–02	–2.053E–15
Fitting Coefficients									
C_6	1.460E–04	–5.950E–18	–5.200E–05	–6.046E–17	C_6	–1.373E–03	5.221E–19	–1.570E–03	–9.805E–17
C_5	8.600E–04	–2.390E–20	–1.223E–03	–9.414E–17	C_5	6.723E–05	–2.050E–18	1.117E–04	8.816E–17
C_4	4.285E–03	2.692E–17	4.993E–03	3.873E–16	C_4	6.427E–03	–6.421E–18	6.732E–03	9.847E–17
C_3	1.297E–02	–1.020E–16	–1.490E–02	–4.064E–16	C_3	–3.607E–04	3.813E–17	–2.938E–04	–2.471E–16
C_2	4.163E–02	1.853E–16	3.873E–02	5.188E–16	C_2	1.928E–02	–5.303E–17	2.090E–02	–3.091E–17
C_1	6.270E–04	–6.860E–16	3.980E–04	–1.064E–15	C_1	–6.655E–06	1.454E–16	–6.128E–05	–2.005E–15
C_0	–2.000E–06	4.099E–19	6.000E–06	–5.511E–20	C_0	2.797E–07	3.639E–19	–5.586E–07	1.708E–18

Mode 5					Mode 6				
	CHDBrI		$CHDBrI^+$			CHDBrI		$CHDBrI^+$	
q[Å]	$V(q)$	$E^{\mathrm{PV}}(q)$	$V(q)$	$E^{\mathrm{PV}}(q)$	q[Å]	$V(q)$	$E^{\mathrm{PV}}(q)$	$V(q)$	$E^{\mathrm{PV}}(q)$
–0.5	3.323E–02	1.990E–15	2.896E–02	3.461E–16	–0.5	2.892E–02	–1.310E–15	2.850E–02	–1.284E–15
–0.4	2.040E–02	1.616E–15	1.771E–02	1.427E–16	–0.4	1.777E–02	–1.093E–15	1.756E–02	–7.730E–16
–0.3	1.091E–02	1.232E–15	9.474E–03	–1.316E–17	–0.3	9.490E–03	–8.495E–16	9.477E–03	–4.013E–16
–0.2	4.600E–03	8.344E–16	4.030E–03	–8.934E–17	–0.2	3.978E–03	–5.823E–16	4.086E–03	–1.550E–16
–0.1	1.090E–03	4.225E–16	9.930E–04	–9.052E–17	–0.1	9.220E–04	–2.965E–16	1.042E–03	–2.426E–17
0	0	3.905E–19	0	–9.433E–21	0	0	3.905E–19	0	–9.433E–21
0.1	1.171E–03	–4.258E–16	8.910E–04	1.945E–16	0.1	1.091E–03	3.002E–16	8.130E–04	–7.562E–17
0.2	4.751E–03	–8.483E–16	3.789E–03	5.223E–16	0.2	4.339E–03	5.946E–16	3.617E–03	–2.601E–16
0.3	1.110E–02	–1.259E–15	9.033E–03	1.024E–15	0.3	1.007E–02	8.753E–16	8.758E–03	–5.616E–16
0.4	2.058E–02	–1.648E–15	1.702E–02	1.773E–15	0.4	1.860E–02	1.137E–15	1.660E–02	–1.004E–15
0.5	3.333E–02	–2.011E–15	2.800E–02	2.872E–15	0.5	3.005E–02	1.372E–15	2.736E–02	–1.627E–15
Fitting Coefficients									
C_6	–3.714E–03	–3.929E–18	–3.034E–03	–1.258E–18	C_6	–3.323E–03	–6.636E–18	–3.243E–03	–3.644E–18
C_5	–1.100E–05	–3.787E–17	2.230E–04	2.304E–16	C_5	–2.900E–05	2.757E–17	1.690E–04	–7.101E–17
C_4	9.826E–03	5.709E–17	9.126E–03	3.972E–16	C_4	8.587E–03	4.563E–19	9.046E–03	–2.251E–16
C_3	–1.820E–04	1.843E–16	–4.810E–04	4.624E–16	C_3	1.880E–04	–2.120E–16	–1.490E–04	1.600E–17
C_2	3.147E–02	–6.037E–17	2.617E–02	1.449E–15	C_2	2.801E–02	3.957E–17	2.580E–02	–1.427E–15
C_1	2.250E–04	–2.252E–15	–2.560E–04	7.401E–16	C_1	4.500E–04	1.587E–15	–6.040E–04	–1.390E–16
C_0	–5.000E–06	4.561E–19	–3.000E–06	1.828E–19	C_0	–4.000E–06	4.416E–19	–4.000E–06	8.176E–19

Mode 7					Mode 8				
	CHDBrI		$CHDBrI^+$			CHDBrI		$CHDBrI^+$	
q[Å]	$V(q)$	$E^{\mathrm{PV}}(q)$	$V(q)$	$E^{\mathrm{PV}}(q)$	q[Å]	$V(q)$	$E^{\mathrm{PV}}(q)$	$V(q)$	$E^{\mathrm{PV}}(q)$
–0.5	3.514E–02	3.111E–16	3.512E–02	–1.275E–15	–0.5	8.333E–02	9.010E–18	8.515E–02	2.343E–15
–0.4	2.237E–02	2.594E–16	2.222E–02	–9.086E–16	–0.4	6.280E–02	1.134E–17	6.385E–02	1.714E–15
–0.3	1.250E–02	2.000E–16	1.232E–02	–6.071E–16	–0.3	4.200E–02	9.918E–18	4.251E–02	1.165E–15
–0.2	5.542E–03	1.350E–16	5.412E–03	–3.561E–16	–0.2	2.245E–02	6.867E–18	2.262E–02	7.022E–16
–0.1	1.396E–03	6.780E–17	1.344E–03	–1.563E–16	–0.1	6.837E–03	3.287E–18	6.855E–03	3.225E–16
0	0	3.905E–19	0	–9.433E–21	0	0	3.905E–19	0	–9.433E–21
0.1	1.403E–03	–6.564E–17	1.391E–03	1.171E–16	0.1	1.063E–02	2.687E–19	1.062E–02	–2.696E–16
0.2	5.751E–03	–1.292E–16	5.660E–03	1.992E–16	0.2	5.456E–02	5.323E–18	5.431E–02	–4.966E–16
0.3	1.325E–02	–1.894E–16	1.302E–02	2.494E–16	0.3	1.614E–01	2.540E–17	1.601E–01	–6.775E–16
0.4	2.401E–02	–2.454E–16	2.362E–02	2.769E–16	0.4	3.890E–01	4.732E–17	3.845E–01	–8.162E–16
0.5	3.799E–02	–2.968E–16	3.744E–02	2.956E–16	0.5	8.556E–01	8.557E–17	8.428E–01	–8.891E–16
Fitting Coefficients									
C_6	–1.714E–03	3.658E–18	–1.963E–03	1.331E–17	C_6	1.544E–01	1.354E–18	1.495E–01	–6.855E–17
C_5	–8.079E–04	2.474E–18	–6.360E–04	3.787E–17	C_5	2.552E–01	–1.327E–17	2.481E–01	1.095E–16
C_4	3.659E–03	–1.781E–17	4.516E–03	–4.292E–18	C_4	1.793E–01	–1.603E–20	1.766E–01	1.873E–16
C_3	2.477E–03	3.467E–17	1.856E–03	8.855E–17	C_3	2.235E–01	6.733E–17	2.213E–01	–2.785E–16
C_2	3.906E–02	2.057E–17	3.817E–02	–5.556E–16	C_2	2.429E–01	5.206E–17	2.430E–01	7.011E–16
C_1	–5.977E–05	–3.546E–16	7.600E–05	7.218E–16	C_1	5.558E–03	–9.208E–18	5.455E–03	–1.549E–15
C_0	–2.932E–07	3.640E–19	–1.000E–06	3.134E–19	C_0	–1.500E–04	–2.061E–19	–1.450E–04	3.756E–19

Mode 9				
	CHDBrI		$CHDBrI^+$	
q[Å]	$V(q)$	$E^{\mathrm{PV}}(q)$	$V(q)$	$E^{\mathrm{PV}}(q)$
–0.5	6.915E–01	–6.995E–18	6.957E–01	9.798E–16
–0.4	3.234E–01	1.200E–17	3.256E–01	8.659E–16
–0.3	1.373E–01	2.682E–17	1.384E–01	6.981E–16
–0.2	4.722E–02	2.411E–17	4.770E–02	5.002E–16
–0.1	9.326E–03	1.412E–17	9.456E–03	2.652E–16
0	0	3.905E–19	0	–9.433E–21
0.1	6.185E–03	–1.489E–17	6.234E–03	–2.985E–16
0.2	2.048E–02	–2.970E–17	2.075E–02	–6.410E–16
0.3	3.865E–02	–4.283E–17	3.929E–02	–1.024E–15
0.4	5.825E–02	–5.266E–17	5.940E–02	–1.476E–15
0.5	7.786E–02	–5.746E–17	7.969E–02	–1.996E–15
Fitting Coefficients				
C_6	1.029E–01	5.609E–17	1.036E–01	–1.308E–17
C_5	–1.802E–01	–1.667E–17	–1.811E–01	1.849E–17
C_4	1.504E–01	–8.514E–17	1.507E–01	–9.008E–17
C_3	–1.990E–01	7.785E–17	–1.993E–01	–1.128E–16
C_2	2.147E–01	–4.778E–18	2.172E–01	–4.785E–16
C_1	–3.400E–03	–8.277E–17	–3.626E–03	–1.489E–15
C_0	–9.000E–05	–5.081E–20	–9.100E–05	2.324E–19

S6. Orbital contributions analysis for mode 6 of CHDBrI and $CHDBrI^+$

Figure S4 presents the atomic contributions to the total PV energy difference for mode 6 of CHDBrI and $CHDBrI^+$. For both species, the bromine and iodine contributions dominate over the lighter atoms, but we observe a very different behaviour of the two molecules for mode 6. For the cation, the shape of the PV curve exhibits a strong curvature, while for the neutral molecule we see an almost linear behaviour (for the total as well as atomic PV contributions). The latter leads to a very small PV vibrational frequency shift as the second derivative $\partial^2 E^{\mathrm{PV}}/\partial q^2(q=0)$ becomes zero (or close to zero). To understand this different behaviour we further consider the individual molecular orbital (MO) contributions of the two atoms Br and I contributing most to the PV energy shift.

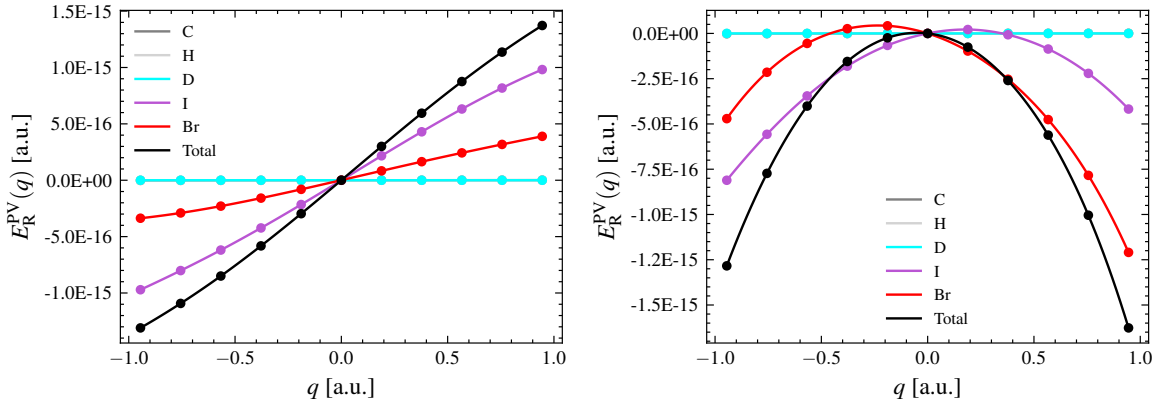

Figure S4: Breakdown of the atomic contributions to the total PV energy $E^{\mathrm{PV}}(q)$ along mode 6 in (R)-CHDBrI (left) and (R)-CHDBrI$^+$ (right).

There are in total 48 occupied MOs in our calculations for CHDBrI. The important MOs that we focus on in our analysis are the HOMO/SOMO (MO 48) and the added orbital contributions from the 47 orbitals up to and including HOMO/SOMO – 1 (MOs 1–47). This breakdown is shown in the top plots of Figure S5. For both CHDBrI and CHDBrI$^+$ we observe, for the PV contributions from MOs 1–47, an almost harmonic PV curve of (approximately) second order in q with bromine being the main contributor to the PV. However, the MO 48 (HOMO/SOMO) contribution shown changes the shape of the total PV curve shown in middle plots of Figure S5 to an odd function of (approximately) third order in q for the neutral molecule, in contrast to the cationic species. This analysis suggests that the removal of a HOMO electron from the neutral molecule makes the contribution from the inner orbitals dominant, which translates into a function that has a stronger curvature. Further support of this argument can be seen from the bottom panels in Figure S5 where i) doubling of the SOMO contribution in the cation (artificial addition of 1 electron) results in a pseudo-neutral system with suppressed curvature in the PV curve (bottom right) resembling the neutral molecule (middle left); ii) halving the HOMO contribution in the neutral system (artificial removal of 1 electron) results in a pseudo-cation with increased curvature of the PV curve (bottom left) resembling the unaltered cation (middle right).

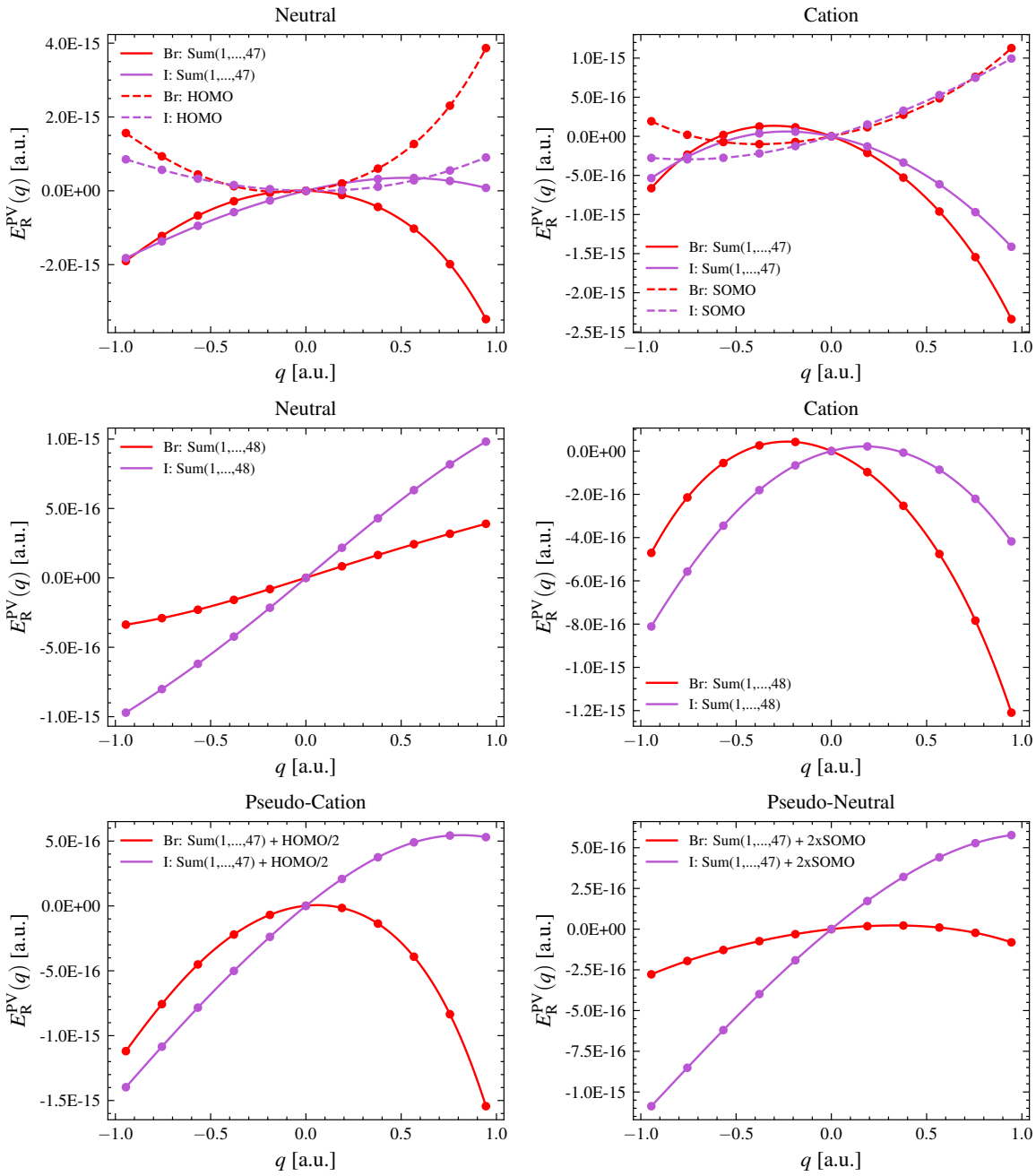

Figure S5: Orbital contributions of PV energies $E^{\mathrm{PV}}(q)$ along mode 6 in the neutral (left) and cation (right) of (R)-CHDBrI. Top: Added PV contributions up to and including the HOMO/SOMO – 1 orbital (MO 47) and separate HOMO/SOMO (MO 48) contribution. Middle: Added PV contributions up to and including MO 48 (HOMO/SOMO). Bottom: Artificial electron removal/addition in (R)-CHDBrI/(R)-CHDBrI$^+$ (left/rigth panel) by means of halving/doubling the HOMO/SOMO (MO 48) contribution.

S7. Chiral Density Analysis

In an attempt to provide rationalization for the observed enhancement of the PV shift in $CHDBrI^+$ compared to the parent CHDBrI molecule, we visualize the changes in the chiral density $\gamma^5(r)$ in the vicinity of Br and I nuclei along the vibrational mode 6 in Figures S6–S11. We show spatial isocontour plots in Figure S7 and break these down into respective radial (Figure S6) and angular parts (Figures S8–S11).

We make several observations. In general, the chiral density exhibits the most structure in the near vicinity of the nucleus in the radial region between 0.001 – 0.01 a.u. (see contour plots in Figure S7). In contrast, the intranuclear region is mostly featureless and practically homogenious (see the leftmost columns in Figures S8–S11 as well as the plateau in the shaded nuclear region of the radial plots in Figure S6). This is also consistent with the insensitivity of the PV energy shifts to the employed nuclear models. Chiral density in the outer region beyond 0.2 a.u. is practically zero and is thus of no importance on the scales of the chemical bonding.

The maximum amplitude of the chiral density is up to 10× larger in the cation as compared to the neutral CHDBrI (note the scales in angular plots and contour values in spatial plots). However, this is mostly observed in the extra-nuclear region. In the intra-nuclear region, the amplitudes of the chiral densities are comparable in both systems. In all cases, the radial distribution (Figure S6) is significantly suppressed in the extra-nuclear region due to the angular averaging of the chiral density structure. This is the case even in $CHDBrI^+$ where the absolute amplitudes outside of the nuclear region are much larger, yet their angular average is still suppressed.

The spatial plots in Figure S7 show the changes in chiral density along the mode are more pronounced in CHDBrI, where the isocontour shapes morph significantly. In $CHDBrI^+$, one can observe slight rotation and subtle changes in the overall shape of the contours. Interestingly, in CHDBrI, the endpoints at $q = -0.5$ Å and $q = 0.5$ Å are practically mirror and sign reflections of one another supporting the close to linear odd-functional behavior of

the $E^{\mathrm{PV}}(q)$ curve in Figure S3 in Section S5. In both systems, the spatial extent of the chiral density contours appear larger around Br as compared to I.

Similar conclusions can be drawn for the chiral density plots in the remaining vibrational modes, we thus omit these for sake of brevity and size of the ESI file. All chiral density visualization calculations were performed using DIRAC19.[25]

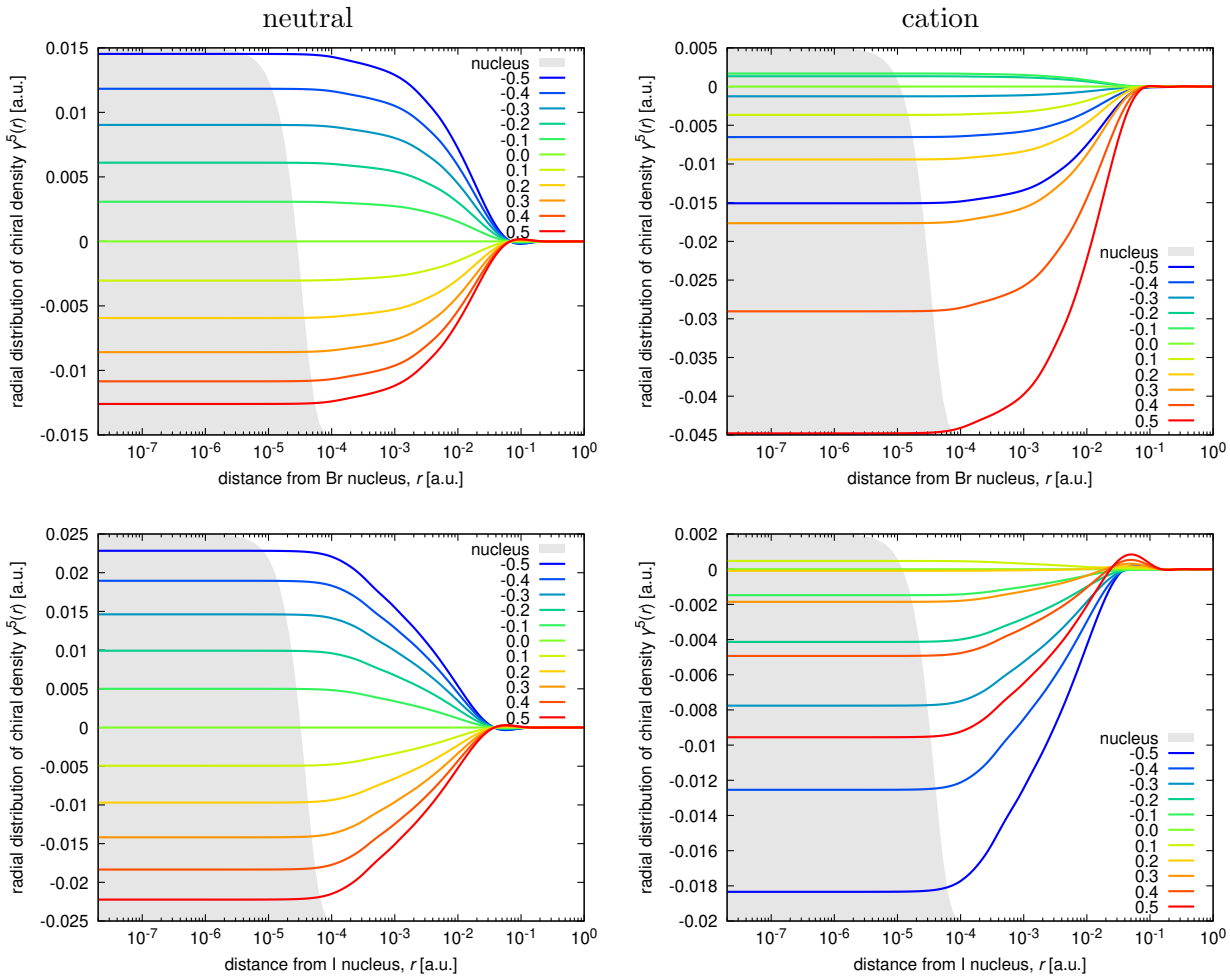

Figure S6: Radial distributions of chiral density $\gamma^5(r)$ (in a.u.) around Br and I nuclei in CHDBrI and $CHDBrI^+$ for displacements between $q \in \langle -0.5, 0.5 \rangle$ Å along vibrational mode 6. Nuclear charge distribution is represented by the grey shaded area.

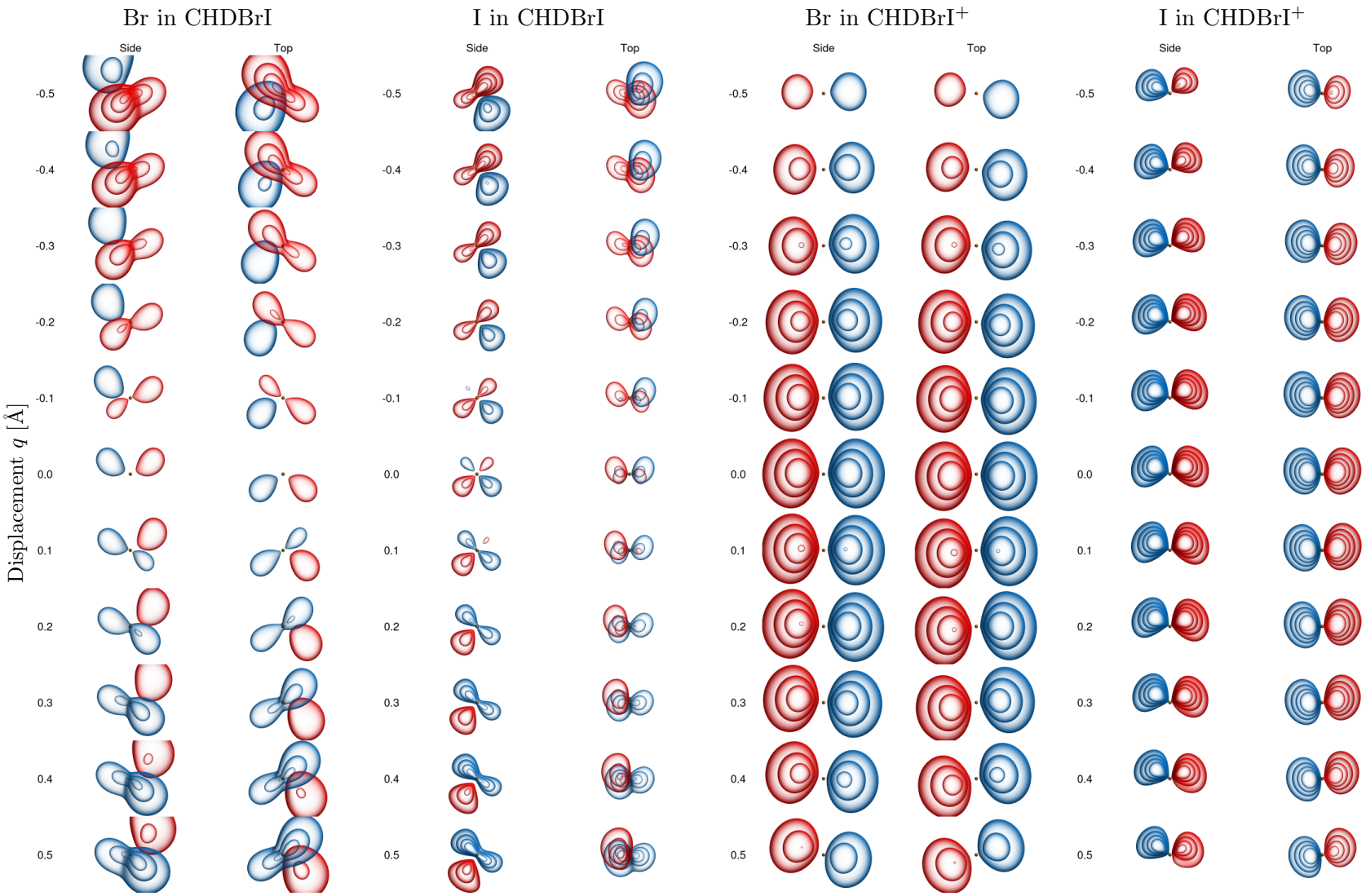

Figure S7: Spatial isocontour plots of chiral density $\gamma^5(r)$ (in a.u.) around the Br and I nuclei for displacements between $q \in \langle -0.5, 0.5 \rangle$ Å along the vibrational mode 6. The width of each plotted box is 0.15 a.u.. Note, the scales for CHDBrI and $CHDBrI^+$ are vastly different – for CHDBrI, we use contour values ± 0.0003, ± 0.0005, ± 0.0007, ± 0.0009 a.u.; for $CHDBrI^+$, we use contour values ± 0.005, ± 0.007, ± 0.009, ± 0.011 a.u.; positive contours are plotted in red, negative in blue.

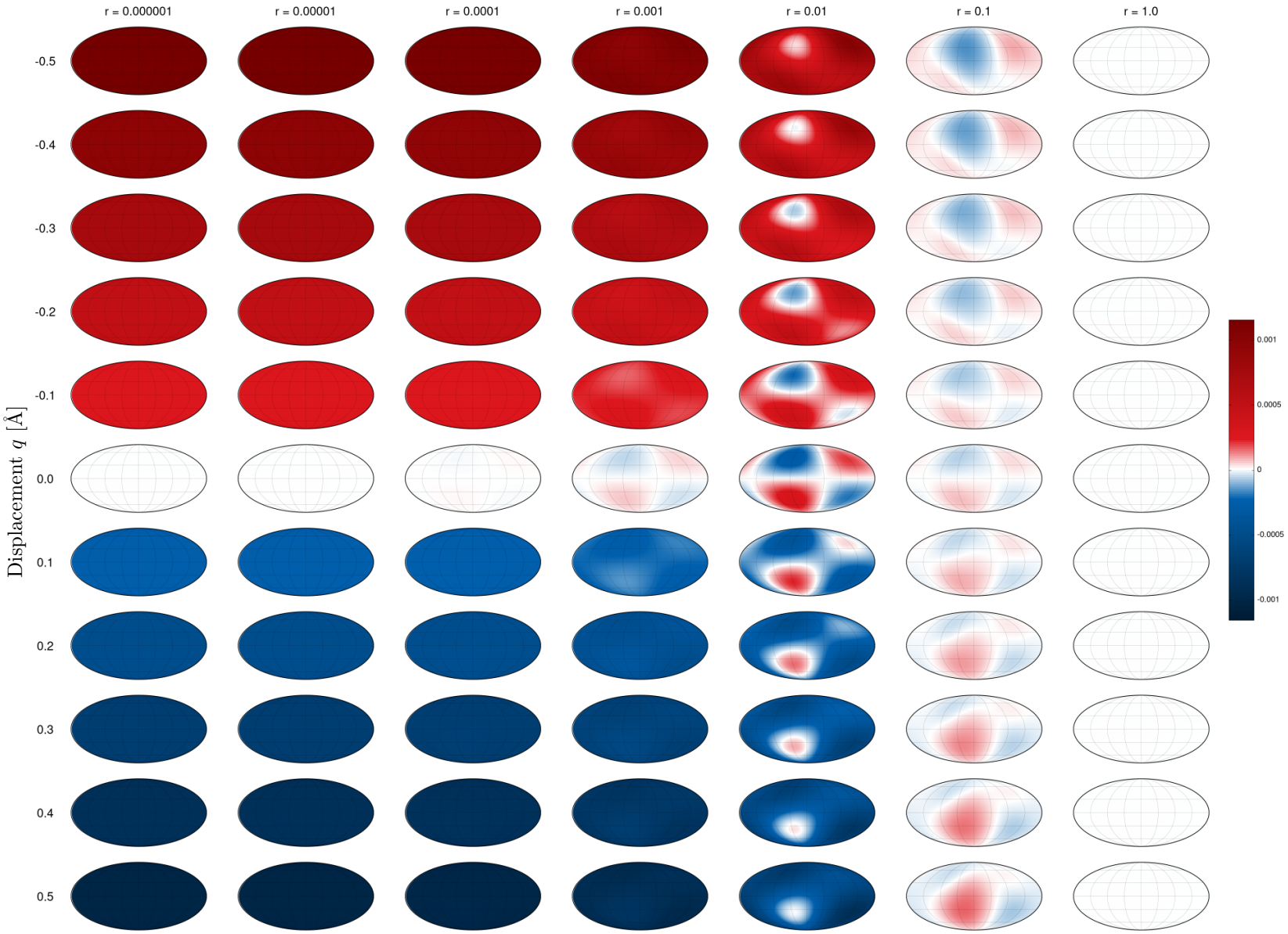

Figure S8: Angular distribution of chiral density $\gamma^5(r)$ (in a.u.) in Mollweide projection over different sized concentric radial shells around the Br nucleus in CHDBrI (columns) for displacements $q \in \langle -0.5, 0.5 \rangle$ Å along vibrational mode 6 (rows).

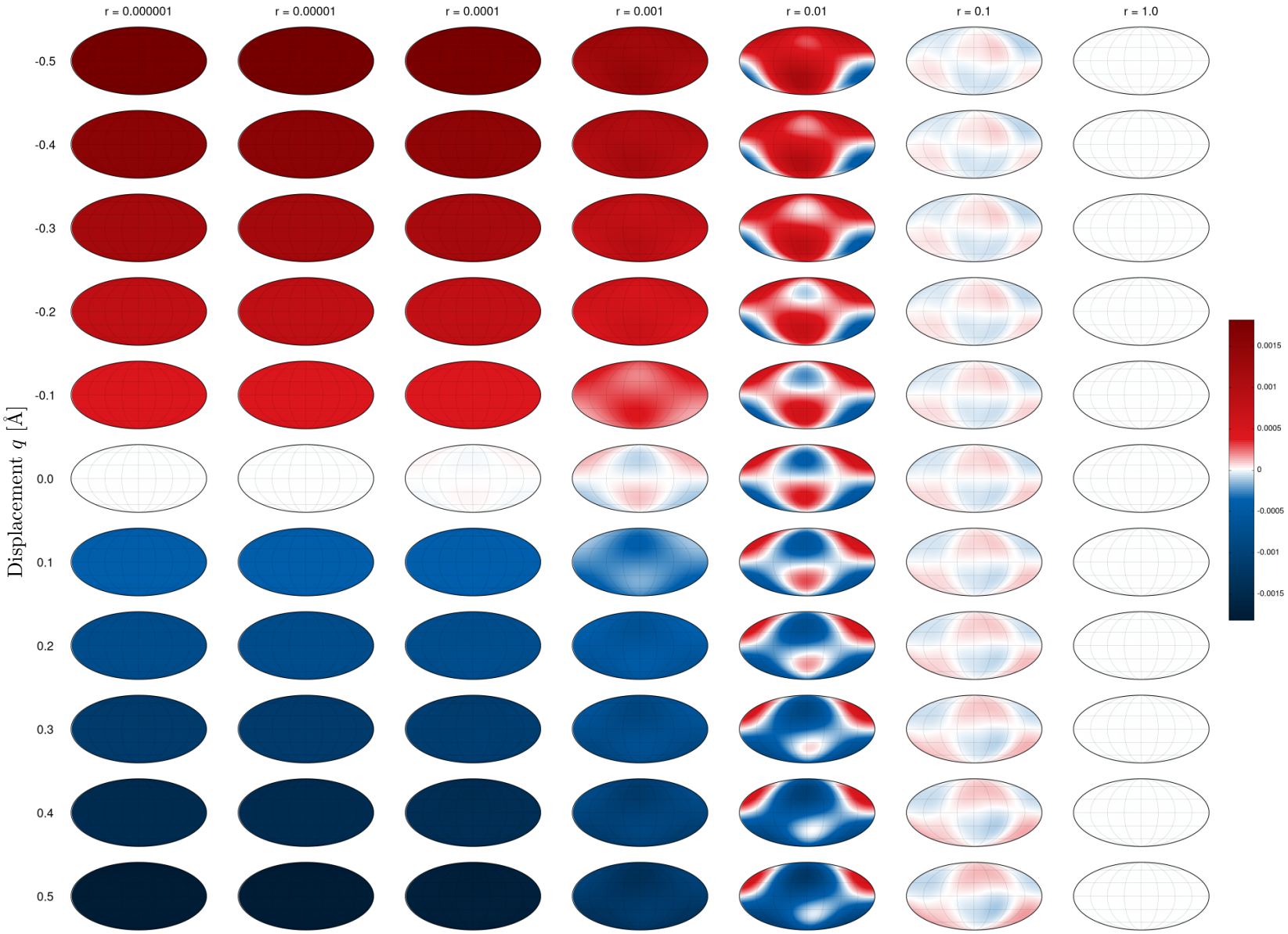

Figure S9: Angular distribution of chiral density $\gamma^5(r)$ (in a.u.) in Mollweide projection over different sized concentric radial shells around the I nucleus in CHDBrI (columns) for displacements $q \in \langle -0.5, 0.5 \rangle$ Å along vibrational mode 6 (rows).

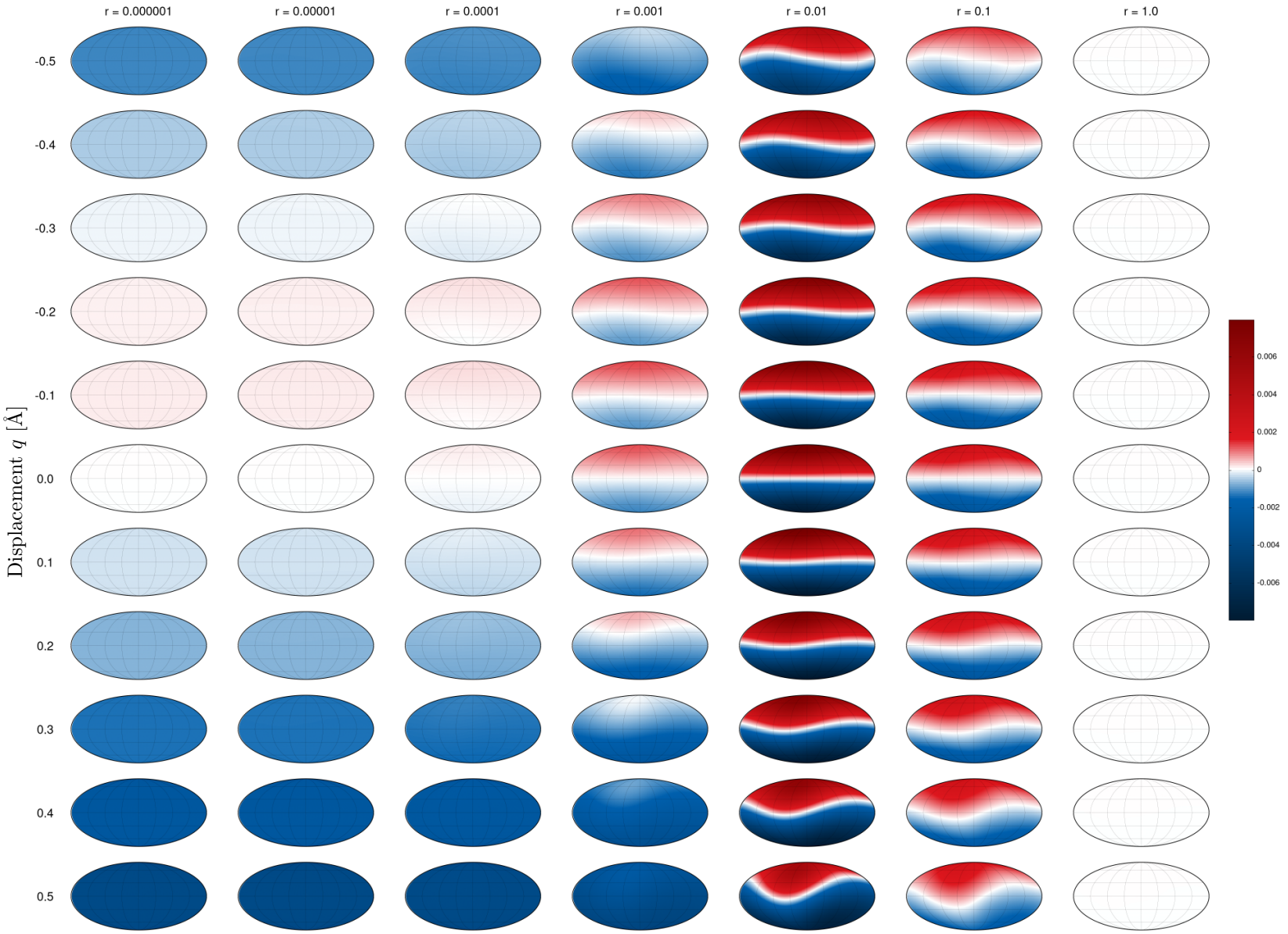

Figure S10: Angular distribution of chiral density $\gamma^5(r)$ (in a.u.) in Mollweide projection over different sized concentric radial shells around the Br nucleus in $CHDBrI^+$ (columns) for displacements $q \in \langle -0.5, 0.5 \rangle$ Å along vibrational mode 6 (rows).

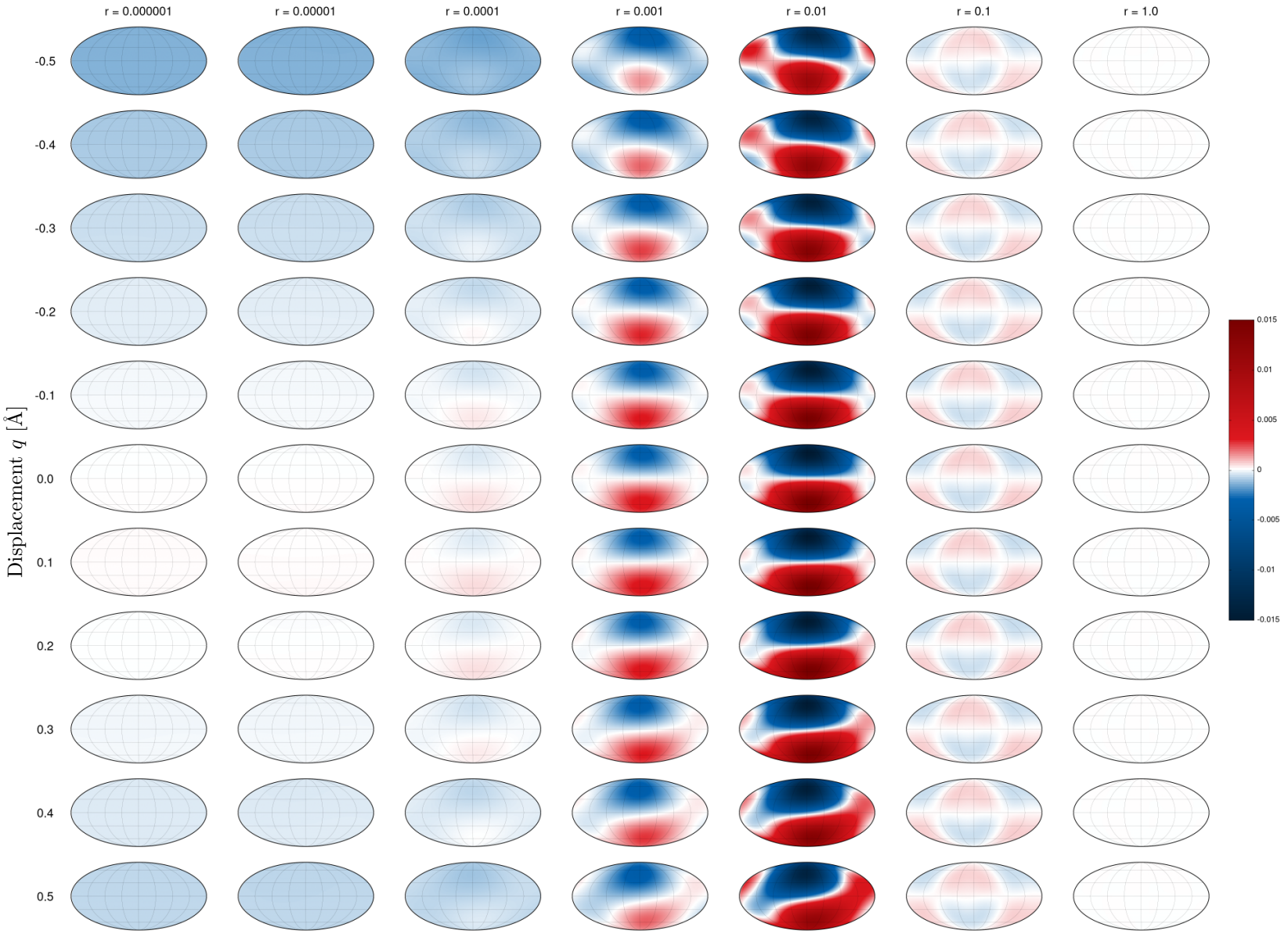

Figure S11: Angular distribution of chiral density $\gamma^5(r)$ (in a.u.) in Mollweide projection over different sized concentric radial shells around the I nucleus in $CHDBrI^+$ (columns) for displacements $q \in \langle -0.5, 0.5 \rangle$ Å along vibrational mode 6 (rows).

S8. Additional Information

Figures S12–S19 show orbital decomposition analysis for modes 1–5 and 7–9 analogous to that of mode 6 shown on Figure S5 and discussed in Section S6. The analysis of the increased and decreased curvature caused by the cancellation effects between MOs 1–47 and MO 48 is however, less applicable in the general case. The effect in mode 5 is very similar to that observed in mode 6 in Figure S5 as both of these modes are similar in nature (C–H and C–D wag, respectively)

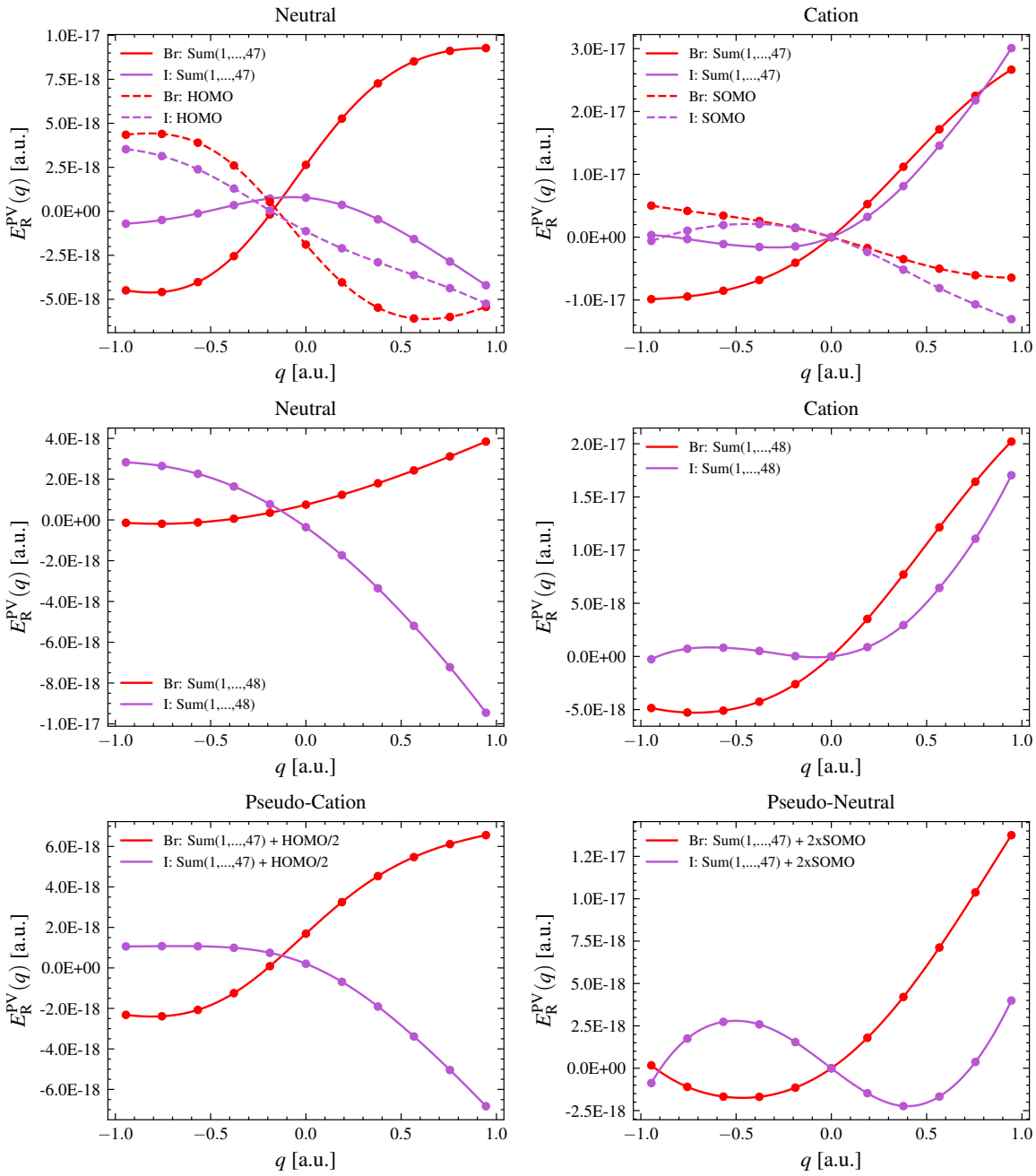

Figure S12: Orbital contributions of PV energies $E^{\mathrm{PV}}(q)$ along mode 1 in the neutral (left) and cation (right) of (R)-CHDBrI. Top: Added PV contributions up to and including the HOMO/SOMO – 1 orbital (MO 47) and separate HOMO/SOMO (MO 48) contribution. Middle: Added PV contributions up to and including MO 48 (HOMO/SOMO). Bottom: Artificial electron removal/addition in (R)-CHDBrI/(R)-CHDBrI$^+$ (left/rigth panel) by means of halving/doubling the HOMO/SOMO (MO 48) contribution.

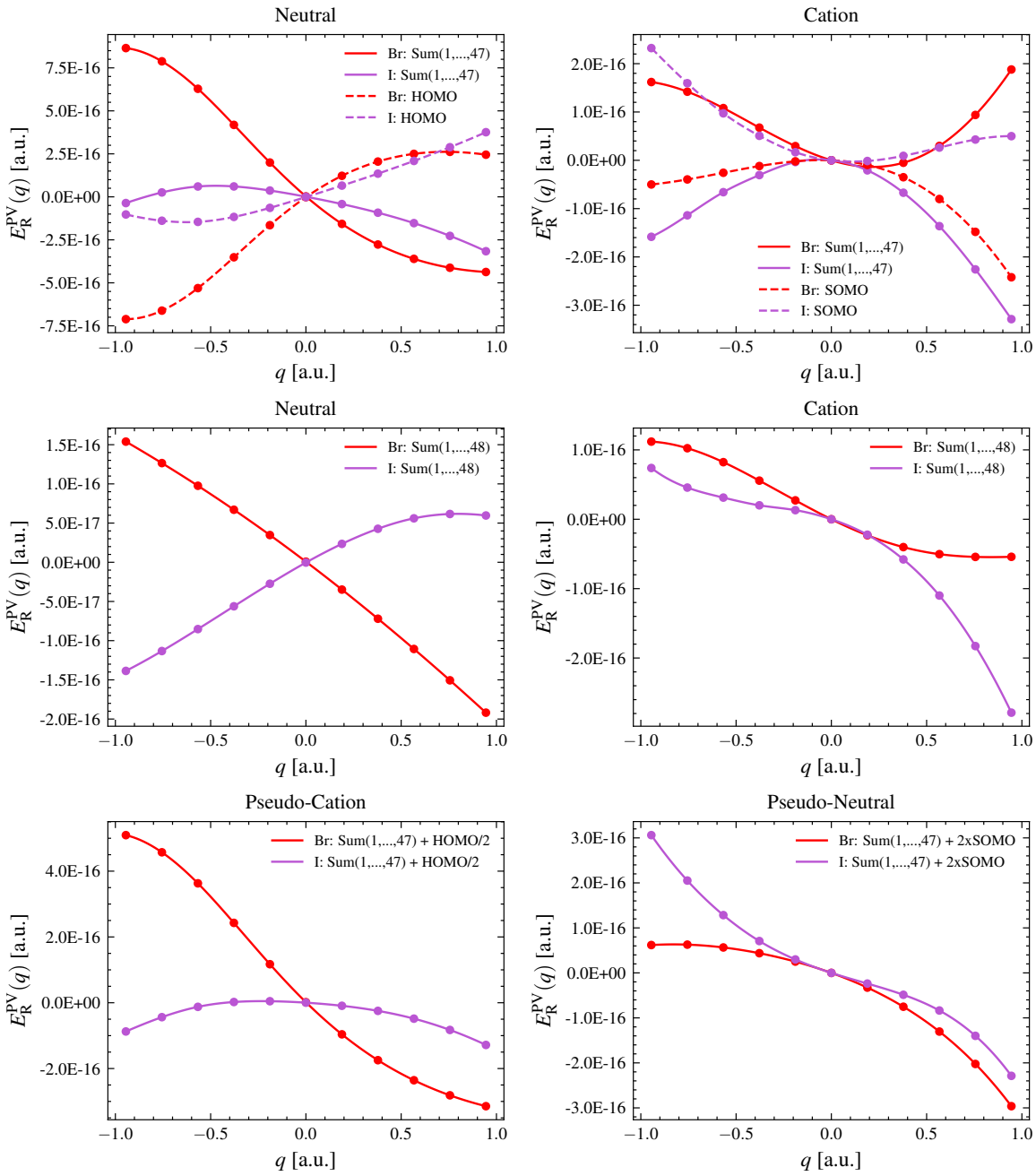

Figure S13: Orbital contributions of PV energies $E^{\mathrm{PV}}(q)$ along mode 2 in the neutral (left) and cation (right) of (R)-CHDBrI. Top: Added PV contributions up to and including the HOMO/SOMO – 1 orbital (MO 47) and separate HOMO/SOMO (MO 48) contribution. Middle: Added PV contributions up to and including MO 48 (HOMO/SOMO). Bottom: Artificial electron removal/addition in (R)-CHDBrI/(R)-CHDBrI$^+$ (left/rigth panel) by means of halving/doubling the HOMO/SOMO (MO 48) contribution.

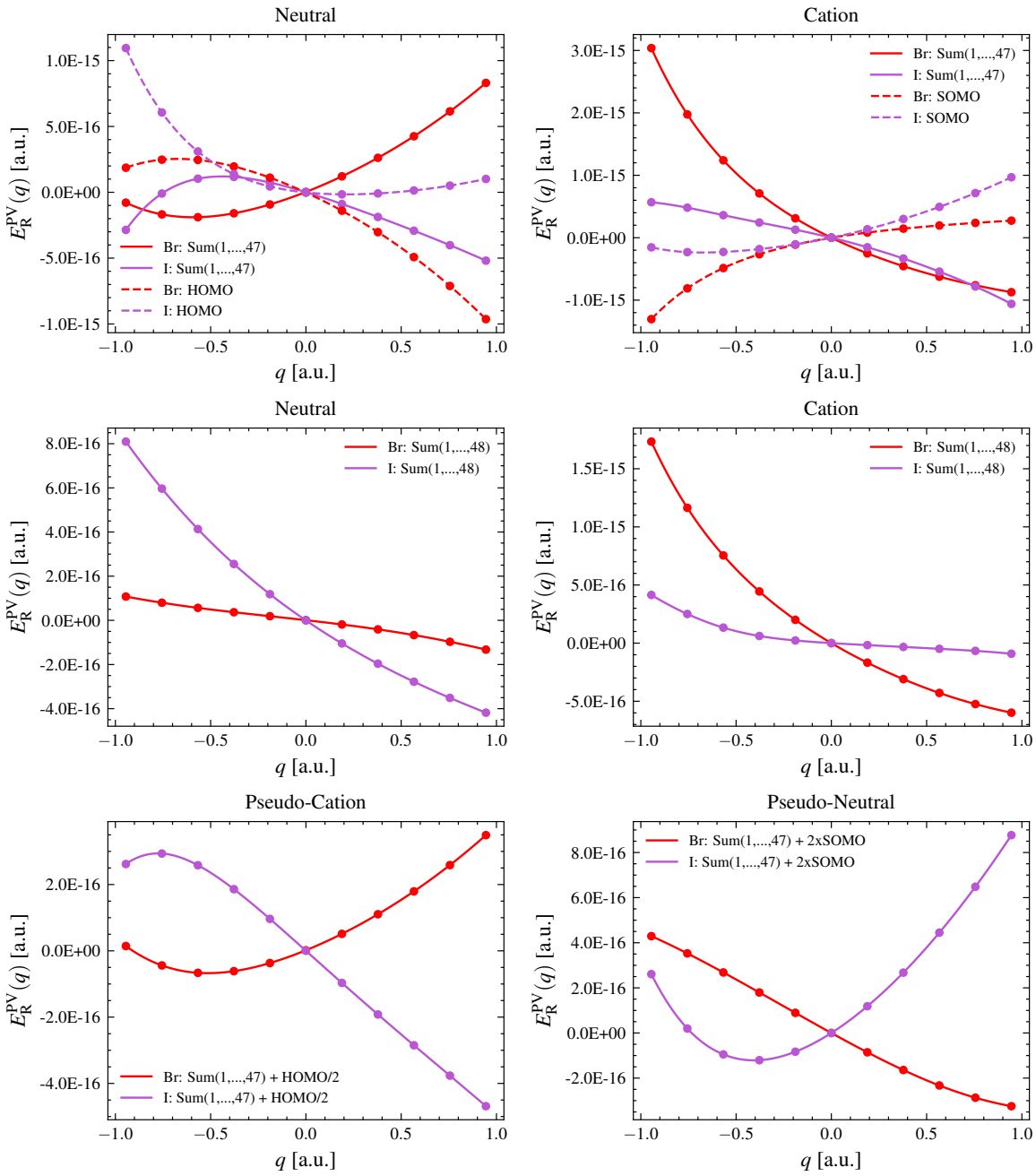

Figure S14: Orbital contributions of PV energies $E^{\mathrm{PV}}(q)$ along mode 3 in the neutral (left) and cation (right) of (R)-CHDBrI. Top: Added PV contributions up to and including the HOMO/SOMO – 1 orbital (MO 47) and separate HOMO/SOMO (MO 48) contribution. Middle: Added PV contributions up to and including MO 48 (HOMO/SOMO). Bottom: Artificial electron removal/addition in (R)-CHDBrI/(R)-CHDBrI$^+$ (left/rigth panel) by means of halving/doubling the HOMO/SOMO (MO 48) contribution.

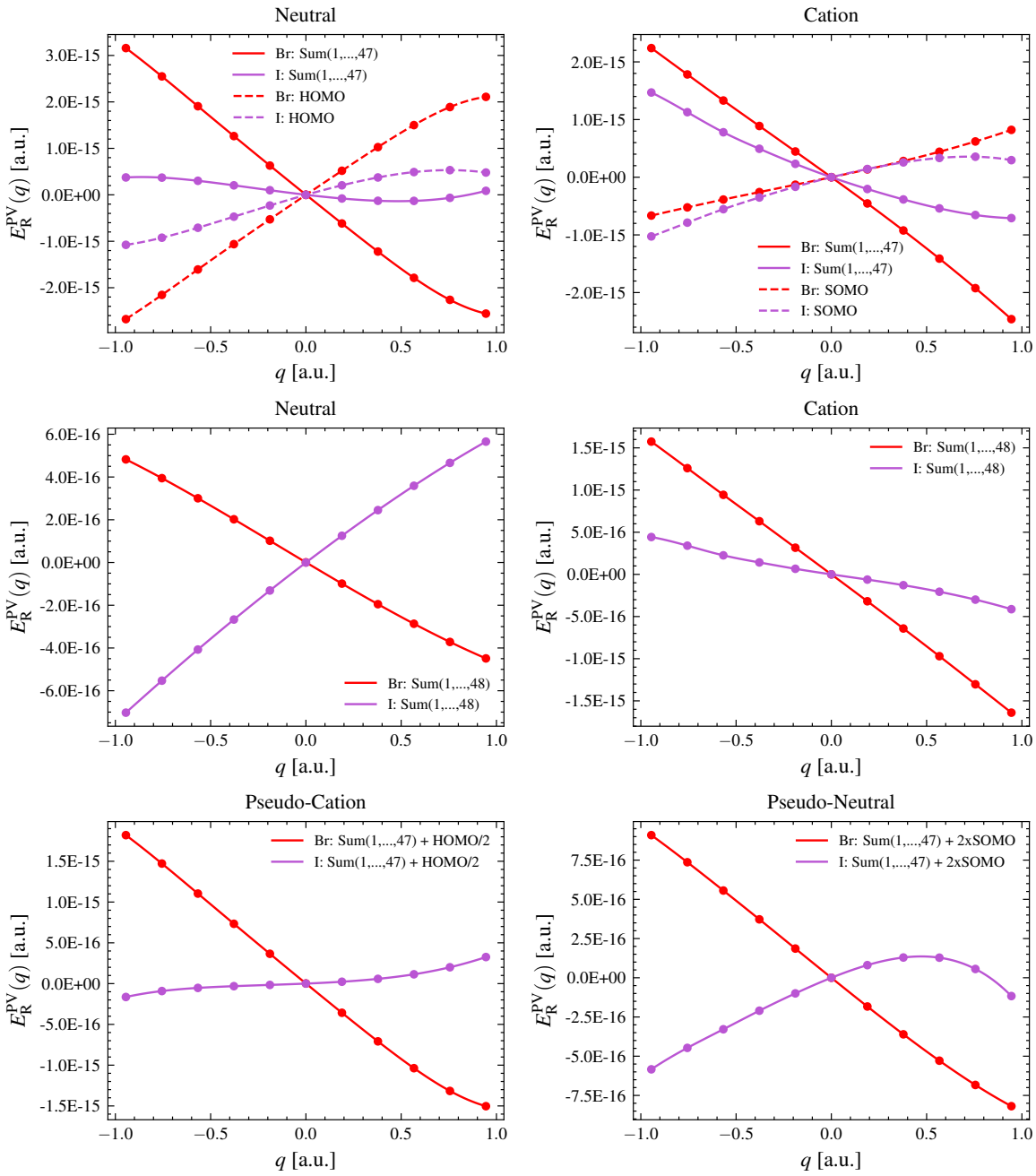

Figure S15: Orbital contributions of PV energies $E^{\mathrm{PV}}(q)$ along mode 4 in the neutral (left) and cation (right) of (R)-CHDBrI. Top: Added PV contributions up to and including the HOMO/SOMO – 1 orbital (MO 47) and separate HOMO/SOMO (MO 48) contribution. Middle: Added PV contributions up to and including MO 48 (HOMO/SOMO). Bottom: Artificial electron removal/addition in (R)-CHDBrI/(R)-CHDBrI$^+$ (left/rigth panel) by means of halving/doubling the HOMO/SOMO (MO 48) contribution.

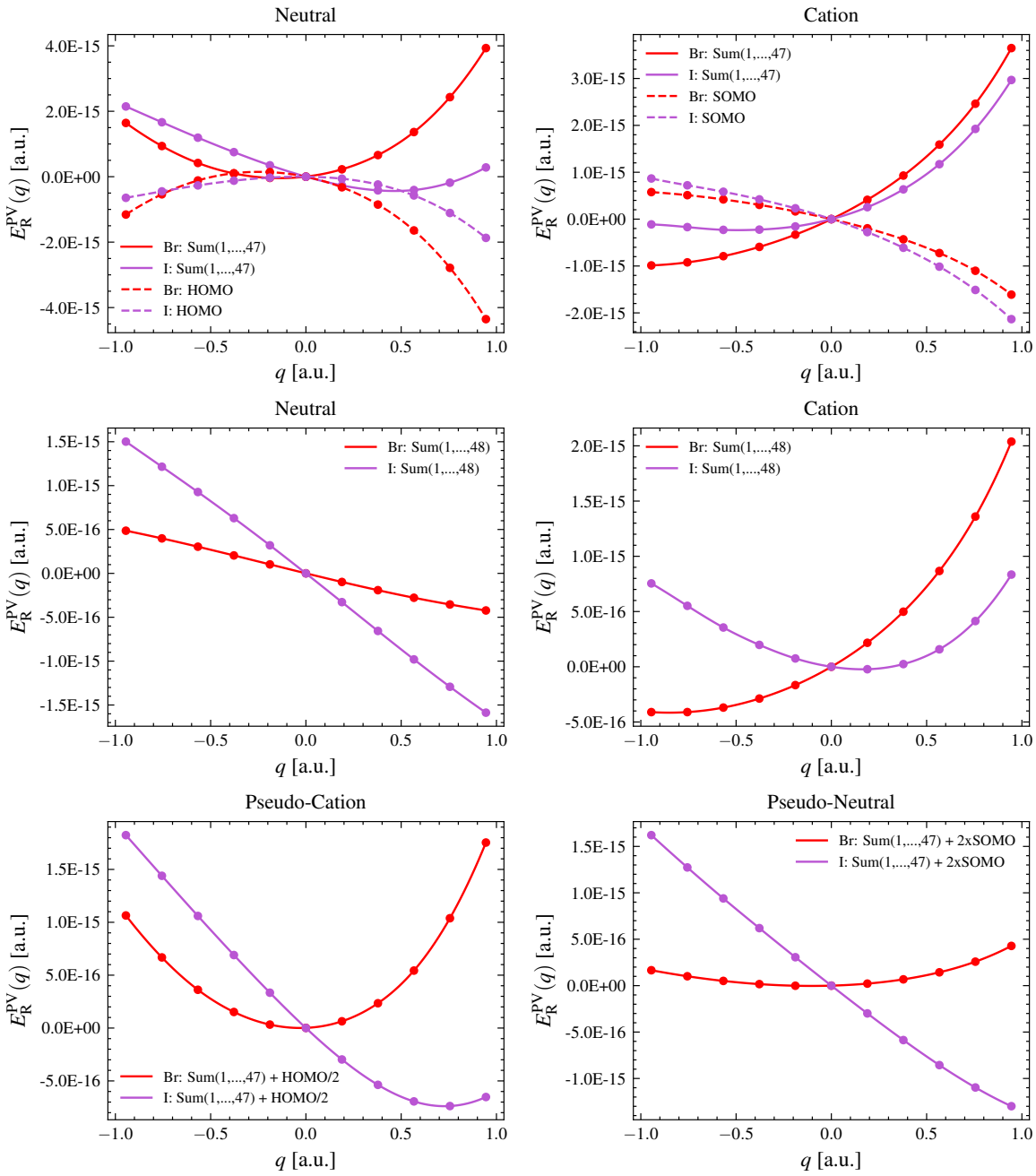

Figure S16: Orbital contributions of PV energies $E^{\mathrm{PV}}(q)$ along mode 5 in the neutral (left) and cation (right) of (R)-CHDBrI. Top: Added PV contributions up to and including the HOMO/SOMO – 1 orbital (MO 47) and separate HOMO/SOMO (MO 48) contribution. Middle: Added PV contributions up to and including MO 48 (HOMO/SOMO). Bottom: Artificial electron removal/addition in (R)-CHDBrI/(R)-CHDBrI$^+$ (left/rigth panel) by means of halving/doubling the HOMO/SOMO (MO 48) contribution.

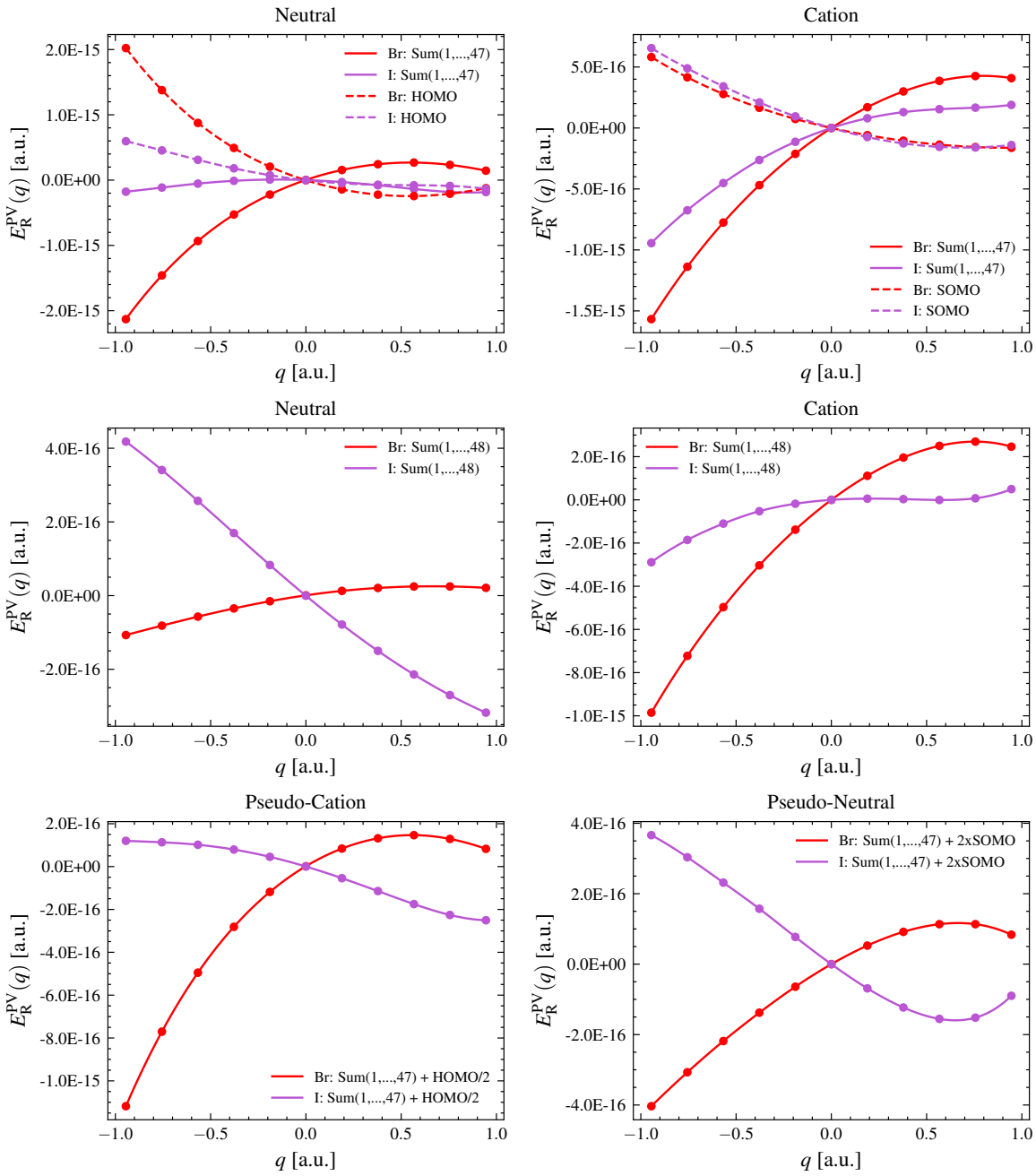

Figure S17: Orbital contributions of PV energies $E^{\mathrm{PV}}(q)$ along mode 7 in the neutral (left) and cation (right) of (R)-CHDBrI. Top: Added PV contributions up to and including the HOMO/SOMO – 1 orbital (MO 47) and separate HOMO/SOMO (MO 48) contribution. Middle: Added PV contributions up to and including MO 48 (HOMO/SOMO). Bottom: Artificial electron removal/addition in (R)-CHDBrI/(R)-CHDBrI$^+$ (left/rigth panel) by means of halving/doubling the HOMO/SOMO (MO 48) contribution.

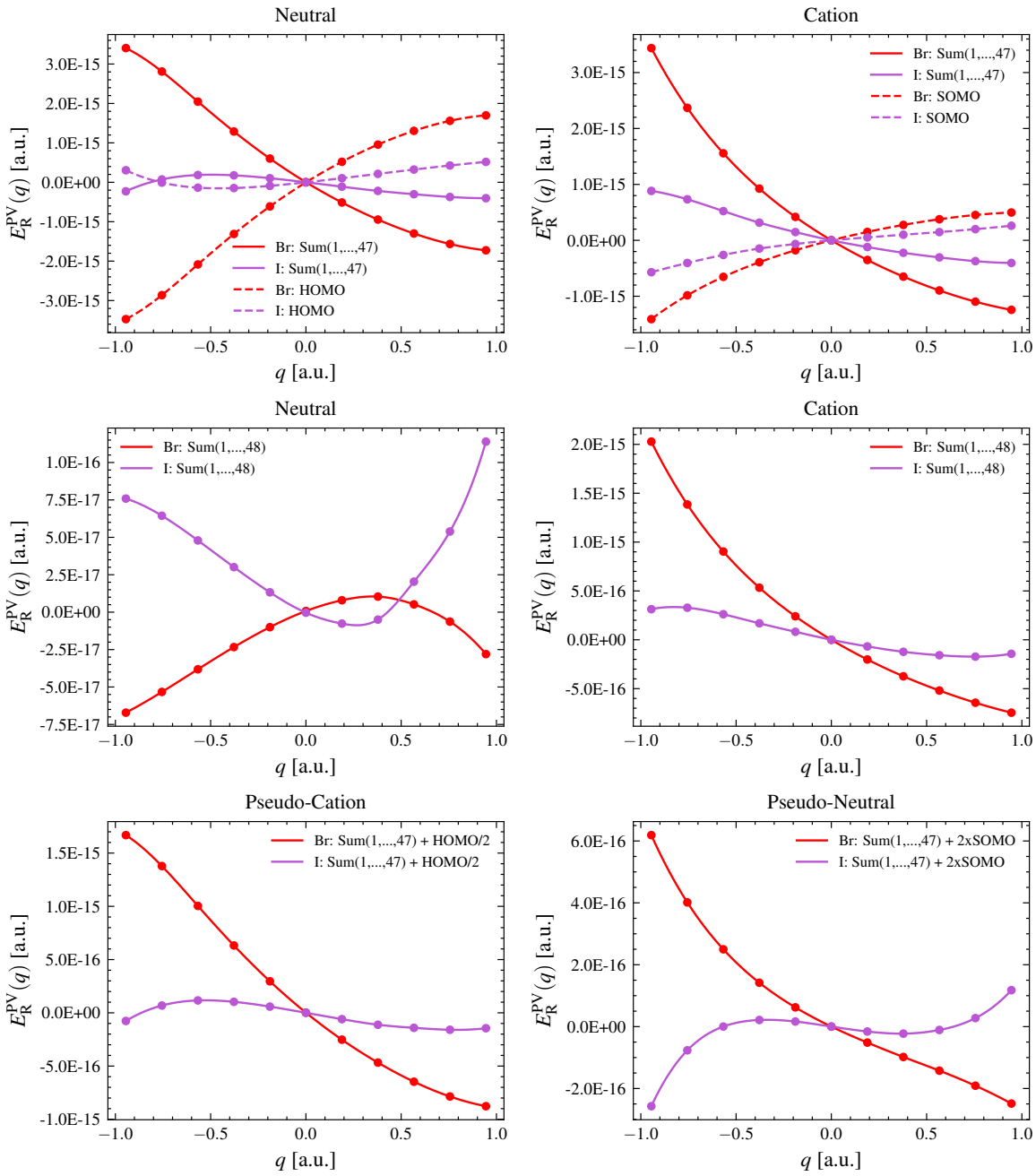

Figure S18: Orbital contributions of PV energies $E^{\mathrm{PV}}(q)$ along mode 8 in the neutral (left) and cation (right) of (R)-CHDBrI. Top: Added PV contributions up to and including the HOMO/SOMO – 1 orbital (MO 47) and separate HOMO/SOMO (MO 48) contribution. Middle: Added PV contributions up to and including MO 48 (HOMO/SOMO). Bottom: Artificial electron removal/addition in (R)-CHDBrI/(R)-CHDBrI$^+$ (left/rigth panel) by means of halving/doubling the HOMO/SOMO (MO 48) contribution.

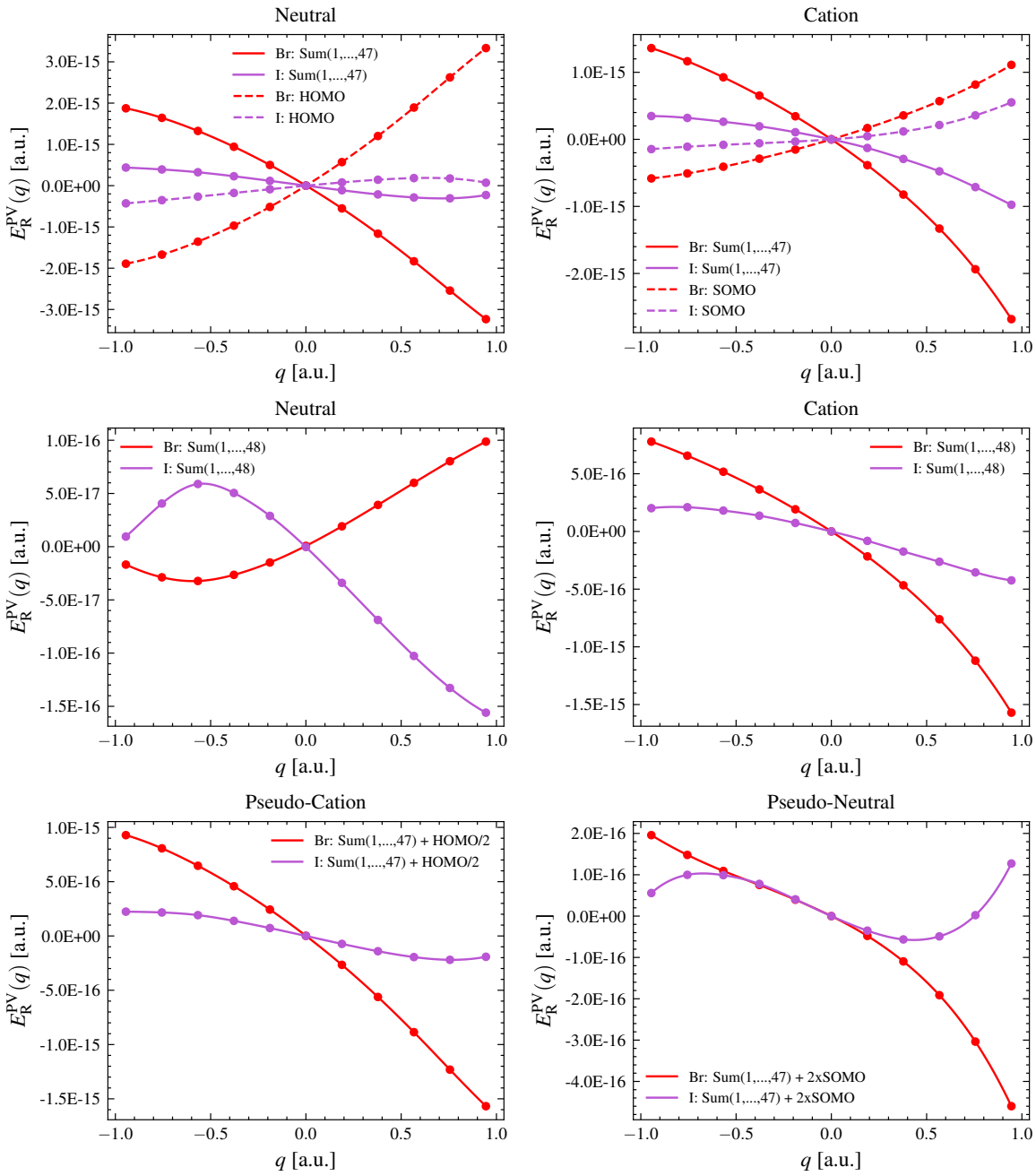

Figure S19: Orbital contributions of PV energies $E^{\mathrm{PV}}(q)$ along mode 9 in the neutral (left) and cation (right) of (R)-CHDBrI. Top: Added PV contributions up to and including the HOMO/SOMO – 1 orbital (MO 47) and separate HOMO/SOMO (MO 48) contribution. Middle: Added PV contributions up to and including MO 48 (HOMO/SOMO). Bottom: Artificial electron removal/addition in (R)-CHDBrI/(R)-CHDBrI$^+$ (left/rigth panel) by means of halving/doubling the HOMO/SOMO (MO 48) contribution.

References

(1) Clabo, D.; Allen, W. D.; Remington, R. B.; Yamaguchi, Y.; Schaefer, H. F. A systematic study of molecular vibrational anharmonicity and vibration—rotation interaction by self-consistent-field higher-derivative methods. Asymmetric top molecules. *Chemical Physics* **1988**, *123*, 187–239.

(2) Barone, V. Anharmonic vibrational properties by a fully automated second-order perturbative approach. *The Journal of Chemical Physics* **2004**, *122*, 014108.

(3) Carbonniere, P.; Lucca, T.; Pouchan, C.; Rega, N.; Barone, V. Vibrational computations beyond the harmonic approximation: Performances of the B3LYP density functional for semirigid molecules. *Journal of Computational Chemistry* **2005**, *26*, 384–388.

(4) Rauhut, G.; Barone, V.; Schwerdtfeger, P. Vibrational analyses for CHFClBr and CDFClBr based on high level *ab initio* calculations. *The Journal of Chemical Physics* **2006**, *125*, 054308.

(5) Thierfelder, C.; Rauhut, G.; Schwerdtfeger, P. Relativistic coupled-cluster study of the parity-violation energy shift of CHFClBr. *Physical Review A* **2010**, *81*, 032513.

(6) Epifanovsky, E. et al. Software for the frontiers of quantum chemistry: An overview of developments in the Q-Chem 5 package. *The Journal of Chemical Physics* **2021**, *155*, 084801, 084801.

(7) Mardirossian, N.; Head-Gordon, M. ωB97M-V: A combinatorially optimized, range-separated hybrid, meta-GGA density functional with VV10 nonlocal correlation. *The Journal of Chemical Physics* **2016**, *144*, 214110.

(8) Rappoport, D.; Furche, F. Property-optimized Gaussian basis sets for molecular response calculations. *The Journal of Chemical Physics* **2010**, *133*, 134105.

(9) Frisch, M. J. et al. Gaussian˜16 Revision C.01. 2016; Gaussian Inc. Wallingford CT.

(10) Werner, H.-J.; Knowles, P. J.; Knizia, G.; Manby, F. R.; Schütz, M. Molpro: a general-purpose quantum chemistry program package. *Wiley Interdisciplinary Reviews: Computational Molecular Science* **2011**, *2*, 242–253.

(11) Berger, R. In *Relativistic Electronic Structure Theory*; Schwerdtfeger, P., Ed.; Theoretical and Computational Chemistry; Elsevier, 2004; Vol. 14; pp 188–288.

(12) Heß, B. A.; Marian, C. M.; Wahlgren, U.; Gropen, O. A mean-field spin-orbit method applicable to correlated wavefunctions. *Chemical Physics Letters* **1996**, *251*, 365–371.

(13) Schimmelpfennig, B. AMFI, an atomic mean-field spin-orbit integral program. 1996 and 1999; University of Stockholm.

(14) Dyall, K. G. Relativistic Quadruple-Zeta and Revised Triple-Zeta and Double-Zeta Basis Sets for the 4p, 5p, and 6p Elements. *Theoretical Chemistry Accounts* **2006**, *115*, 441–447.

(15) DIRAC, a relativistic ab initio electronic structure program, Release DIRAC23 (2023), written by R. numerov, A. S. P. Gomes, T. Saue and L. Visscher and H. J. Aa. Jensen, with contributions from I. A. Aucar, V. Bakken, C. Chibueze, J. Creutzberg, K. G. Dyall, S. Dubillard, U. Ekström, E. Eliav, T. Enevoldsen, E. Faßhauer, T. Fleig, O. Fossgaard, L. Halbert, E. D. Hedegård, T. Helgaker, B. Helmich–Paris, J. Henriksson, M. van Horn, M. Iliaš, Ch. R. Jacob, S. Knecht, S. Komorovský, O. Kullie, J. K. Lærdahl, C. V. Larsen, Y. S. Lee, N. H. List, H. S. Nataraj, M. K. Nayak, P. Norman, A. Nyvang, G. Olejniczak, J. Olsen, J. M. H. Olsen, A. Papadopoulos, Y. C. Park, J. K. Pedersen, M. Pernpointner, J. V. Pototschnig, R. di Remigio, M. Repisky, K. Ruud, P. Sałek, B. Schimmelpfennig, B. Senjean, A. Shee, J. Sikkema, A. Sunaga, A. J. Thorvaldsen, J. Thyssen, J. van Stralen, M. L. Vidal, S. Villaume, O. Visser, T. Winther, S. Yamamoto and X. Yuan (available at `https://doi.org/10.5281/zenodo.7670749`, see also `https://www.diracprogram.org`).

(16) Noumerov, B. V. A Method of Extrapolation of Perturbations. *Monthly Notices of the Royal Astronomical Society* **1924**, *84*, 592–602.

(17) Cooley, J. W. An Improved Eigenvalue Corrector Formula for Solving the Schrodinger Equation for Central Fields. *Mathematics of Computation* **1961**,

(18) Bast, R. Numerov v0.5.0. `https://doi.org/10.5281/zenodo.1000406`, 2017.

(19) Schwerdtfeger, P.; Saue, T.; van Stralen, J. N. P.; Visscher, L. Relativistic second-order many-body and density-functional theory for the parity-violation contribution to the C–F stretching mode in CHFClBr. *Physical Review A* **2005**, *71*, 012103.

(20) Rauhut, G.; Schwerdtfeger, P. Parity-violation effects in the vibrational spectra of CHFClBr and CDFClBr. *Physical Review A* **2021**, *103*, 042819.

(21) Bailleux, S.; Duflot, D.; Taniguchi, K.; Sakai, S.; Ozeki, H.; Okabayashi, T.; Bailey, W. C. Fourier Transform Microwave and Millimeter-Wave Spectroscopy of Bromoiodomethane, CH_2BrI. *The Journal of Physical Chemistry A* **2014**, *118*, 11744–11750.

(22) El-Sabban, M. Z.; Danti, A.; Zwolinski, B. J. Normal-Coordinate Analysis and Molecular Properties of Four CH_2XY Halomethanes (X = F or I; Y = Cl or Br). *The Journal of Chemical Physics* **1966**, *44*, 1770–1779.

(23) Wu, T. Systematics in the Vibrational Spectra of the Halogen Derivatives of Methane. *The Journal of Chemical Physics* **2004**, *10*, 116–124.

(24) Fiechter, M. R.; Haase, P. A. B.; Saleh, N.; Soulard, P.; Tremblay, B.; Havenith, R. W. A.; Timmermans, R. G. E.; Schwerdtfeger, P.; Crassous, J.; Darquié, B.; Pašteka, L. F.; Borschevsky, A. Toward Detection of the Molecular Parity Violation in Chiral $Ru(acac)_3$ and $Os(acac)_3$. *The Journal of Physical Chemistry Letters* **2022**, *13*, 10011–10017.

(25) 2019; DIRAC, a relativistic ab initio electronic structure program, Release DIRAC19, written by A. S. P. Gomes, T. Saue, L. Visscher, H. J. Aa. Jensen, and R. Bast, with contributions from I. A. Aucar, V. Bakken, K. G. Dyall, S. Dubillard, U. Ekström, E. Eliav, T. Enevoldsen, E. Faßhauer, T. Fleig, O. Fossgaard, L. Halbert, E. D. Hedegård, B. Heimlich–Paris, T. Helgaker, J. Henriksson, M. Iliaš, Ch. R. Jacob, S. Knecht, S. Komorovský, O. Kullie, J. K. Lærdahl, C. V. Larsen, Y. S. Lee, H. S. Nataraj, M. K. Nayak, P. Norman, G. Olejniczak, J. Olsen, J. M. H. Olsen, Y. C. Park, J. K. Pedersen, M. Pernpointner, R. di Remigio, K. Ruud, P. Sałek, B. Schimmelpfennig, B. Senjean, A. Shee, J. Sikkema, A. J. Thorvaldsen, J. Thyssen, J. van Stralen, M. L. Vidal, S. Villaume, O. Visser, T. Winther, and S. Yamamoto (available at uurlhttp://dx.ddoi.org/10.5281/zenodo.3572669, see also uurlhttp://www.diracprogram.org).